KU LEUVEN

FACULTY OF SCIENCE

Investigation of nuclear charge radii of neutron-rich zinc isotopes crossing N=50

Elise SMETS

CERN-THESIS-2024-233
28/06/2024

Supervisor: Prof. G. Neyens
Kern- en Stralingsfysica (IKS)

Co-supervisor: Prof. A. Koszorús
Kern- en Stralingsfysica (IKS)

Mentor: Bram van den Borne
Kern- en Stralingsfysica (IKS)

Thesis presented in
fulfillment of the requirements
for the degree of Master of Science
in Physics

Academic year 2023-2024

Preface

> *"Scientists in their laboratory are not mere technicians: they are also children confronting natural phenomena that impress them as though they were fairy tales"*
>
> *– Marie Skłodowska-Curie*

Already from a young age, I have been fascinated by the wonders of physics. Completing my master's degree in Physics with a dissertation in the enchanting field of nuclear physics is thus a dream come true. Last year, I was able to witness the working of big collaborations and I even got the opportunity to participate in an experiment at CERN. There are an endless amount of people that I want to thank for supporting and guiding me through this period.

Thank you to my boyfriend Jesse for being my rock and my inspiration. Your positive attitude and encouragement have motivated me to keep pushing forward, and I could not have done this without you. Your meticulous eye for detail saved me from embarrassing typos and grammar mishaps, so also a thank you for proofreading this dissertation.

Thank you to my supervisor Gerda Neyens and my co-supervisor Agi Koszorús for their guidance and feedback throughout the year. Your expertise and mentorship have been invaluable in shaping my research journey. On top of that, I want to express my gratitude for providing me with the opportunity to go to CERN and experience the working of the CRIS collaboration myself. I also want to thank Bram, who patiently assisted me with my questions throughout this process.

Thank you to my loving family and my supportive friends. Mama, papa, Thomas, bedankt voor jullie steun en fierheid. Lies, Babet, Tijmen, Charlotte, Thomas, Junan en Caro, bedankt om van Leuven mijn tweede thuis te maken. Thank you to all my family and friends for being my cheering squad and for always being there to celebrate my milestones, big and small.

Abstract

The nuclear shell model is a well-established framework that has consistently demonstrated its ability to reproduce and predict nuclear properties across a wide range of nuclei. Over many years, it has proven to be a powerful tool for describing and forecasting the behavior of nuclei in multiple regions of the nuclear chart, especially its prediction of magic numbers. Magic numbers (2, 8, 20, 28, 50, ...) are the amount of either protons or neutrons that correspond to a completely filled shell followed by a large energy gap. However, from studying exotic nuclei it is found that these magic numbers change when moving far away from stability. In these radioactive nuclei, the energy levels of single-particle orbits begin to shift due to nucleon-nucleon interactions, a phenomenon known as shell evolution. To gain more knowledge about the nuclear structure and nuclear properties in regions far from stability, it is essential to study exotic nuclei. For this reason, nuclear properties of neutron-rich zinc isotopes have been investigated, with a focus on nuclear charge radii crossing the magic gap N=50, and the determination of the spin of ^{81}Zn.

The technique used to study the neutron-rich zinc isotopes is collinear resonance ionization spectroscopy, performed at the CRIS beam-line in ISOLDE, CERN. From these measurements, hyperfine spectra are obtained from which various nuclear properties are extracted such as spin, magnetic dipole moment, electric quadrupole moment, and mean square charge radii. A detailed overview is given of the analysis of hyperfine spectra which are measured for isotopes of ^{64}Zn up to ^{82}Zn.

Prior to this work, neutron-rich zinc isotopes up to ^{80}Zn have been investigated by the COLLAPS group [13], [16]. In addition to that, the spin of ^{81}Zn is experimentally determined for the first time: $I = 5/2$. This finding indicates that no level inversion takes place for the ground state of ^{81}Zn. Furthermore, the nuclear magnetic and quadrupole moment for this isotope are extracted, with the result of a possible configuration mixing. Finally, the nuclear mean square charge radii are obtained which are in a good agreement with the findings of COLLAPS. A strong kink is observed when crossing N=50, proving a strong shell closure.

Contribution Statement

The data analyzed in this dissertation is obtained from the CRIS collaboration group, with Thomas Cocolios and Xiaofei Yang as spokespersons.

The code to Doppler shift and bin the data was provided by my mentor Bram van den Borne. Moreover, the SATLAS2 package was used to fit the data. Analysis of the data was performed by myself, including the reference centroid fluctuations, and error determination on the reference centroid described in Chapter 5.

The results discussed in Chapter 6 in this dissertation are my findings. In Chapter 6.1, the spin assignment for ^{81}Zn, and the determination of the nuclear moments and g-factor are my work. The interpretation of these results has been done with help of my supervisor prof. Neyens. In Chapter 6.2, the differences in mean square charge radii are determined via the King plot method, performed by myself using the field shift F calculated by Leonid FS-RCCSDT. Furthermore, I investigated the kink parameter at different shell closures for different isotopic chains with guidance from my co-supervisor prof. Koszorús.

Summary for a General Audience

Whether the origin of nuclear physics is dated from Becquerel's and Curie's discovery of radioactivity in the late 1890's, or Rutherford's hypothesis of the existence of the nucleus in 1911, the twentieth century was dominated by both experimental and theoretical work in nuclear physics. Since the arrival of *quantum mechanics*, many new discoveries have been made. However, nuclear physics still lacks a coherent theoretical formulation to understand and explain all observed phenomena. Even after a hundred years of research, nuclear physicists are still trying to put the puzzle together.

We already know what the pieces of the puzzle look like; an *atom* is built out of electrons orbiting around a nucleus. This nucleus is made up of neutrons and protons and the amount of neutrons can vary for each element, referred to as *isotopes*. Nuclear physics studies how protons and neutrons are organized inside nuclei. Experimental evidence led to the discovery that nuclei can be described by a *nuclear shell model*, which states that neutrons and protons are stuck in shells around the center part of the nucleus, just like the layers of an onion. Nuclear scientists have built substantial knowledge about stable nuclei by comparing experimental properties of these nuclei with predictions by the shell model. However, the *nuclear properties* of radioactive nuclei need to be determined in order to fully understand how the protons and neutrons are organized in the nucleus.

Each isotope of an element possesses unique properties different from the isotope of the same element with one fewer or additional neutron. These characteristics can be, for example, the shape and the size of the nucleus. The shape can deviate from a sphere, forming a shape like a pancake or a rugby. The size of the nucleus can also vary when adding or removing neutrons. The latter is investigated in this dissertation for zinc isotopes. The size of the nucleus for isotopes with special amounts of neutrons, so-called *magic numbers*, can lead to a better understanding of the theoretical framework of how a nucleus can exist. This investigation is however only one piece of the puzzle and many more need to be laid to grasp the bigger picture. Once completed, this puzzle will illustrate the formation of all elements in the universe, as it allows physicists to understand how each nucleus can exist.

Exploring nuclear properties is not just about unraveling scientific mysteries - it has also practical applications in various fields, including industry and medicine. For example, radioactive isotopes with very specific properties can be used in nuclear medicine to diagnose and treat cancer. Understanding the complexities of nuclear physics, therefore, not only advances our knowledge of the universe, but also benefits society through technological and medical advancements.

Contents

List of Figures

List of Tables

List of Abbreviations

CEC Charge Exchange Cell. 17, 18, 20, 21

CERN Conseil Européen Pour La Recherche Nucléaire (European Council For Nuclear Research). ii, 1, 15

COLLAPS Collinear Laser Spectroscopy. ii, viii, ix, 7, 29–31, 33–35, 38

CRIS Collinear Resonance Ionization Spectroscopy. ii, iii, vii, 7, 16–18, 20, 21

CRISTAL CRIS Laser Tuning, Acquisition And Logging. 20

EFG Electric Field Gradient. 12

FS Field Shift. 13

FWHM Full Width At Half Maximum. 23, 24

HRS High Resolution Separator. 16

IP Ionization Potential. 19

ISCOOL ISOLDE Cooler. vii, viii, 16, 18–21, 40, 41

ISOLDE Isotope Mass Separator On-line Device. ii, vii, 1, 15, 16, 38

MS Mass Shift. 13

NMR Nuclear Magnetic Resonance. 12

NQR Nuclear Quadrupole Resonance. 12

PDL Pulsed Dye Laser. 19

PSB Proton Synchrotron Booster. 15, 16

RIB Radioactive Ion Beam. 16

RILIS Resonance Ionization Laser Ion Source. 16

List of Symbols

β	Deformation parameter
χ^2_ν	Reduced chi-squared
$\delta\nu$	Isotope shift of the hyperfine structure
$\langle r^2 \rangle$	Nuclear mean-squared charge radius
μ	Nuclear magnetic dipole moment
μ_N	Nuclear magneton
A	Mass number
$A_{l,u}$	Hyperfine A-parameter of the lower (l) and upper (u) state
$B_{l,u}$	Hyperfine B-parameter of the lower (l) and upper (u) state
F	Field shift
F	Hyperfine spin state
g	Nuclear g-factor
H	Hamiltonian
I	Nuclear spin
J	Total electron spin
j	Single particle total angular momentum
l	Single particle orbital angular momentum
M	Mass shift
N	Neutron number
Q	Nuclear electric quadrupole moment
R	Nuclear radius
s	Single particle spin angular momentum
T_i	Kinetic energy of particle i

$V_{i,j}$	Nuclear two-body potential
V_{ls}	Spin-orbit coupling
Z	Atomic number

Chapter 1

Introduction

Whether the origin of nuclear physics is dated from Becquerel's and Curie's discovery of radioactivity in the late 1890's, or Rutherford's hypothesis of the existence of the nucleus in 1911, it is clear that experimental and theoretical work in nuclear physics has been pivotal to the progress of physics throughout the twentieth century. The arrival of quantum physics quickly led to the development of nuclear physics, resulting in many fundamental discoveries, such as the discovery of the neutron by Chadwick. However, nuclear physics still lacks a coherent theoretical formulation that would allow scientists to analyze and interpret all phenomena in a fundamental way. Rather than having a single unifying theory, there are bright sparks of coherent knowledge flickering within the boundless darkness of seemingly random observations.

After more than a hundred years of research, nuclear physicists are still trying to put the puzzle together. A lot of progress has been made to build a comprehensive understanding of the structure and behavior of atomic nuclei. Researchers study the complex interplay between collective and single-particle phenomena that determine the properties of nuclei. This provides insights into the fundamental nuclear forces and the mechanisms of nuclear binding.

Facilities like ISOLDE at CERN are key to these kinds of studies as radioactive ion beams can be produced there. The objective is not merely to complete a partially filled catalog, but to investigate nuclei in regimes far from stability, including the study of phenomena such as halo nuclei and new islands of stability. In addition to the scientific advancements, studying nuclear properties also leads to applications in various fields such as industry and medicine. For instance, facilities producing radioactive ion beams investigate and create radioactive isotopes used in nuclear medicine to diagnose and treat cancer.

Furthermore, the study of nuclear properties is omnipresent in the field of nuclear astrophysics. The abundance of nuclei in the primordial universe and stellar nucleosynthesis are brought together with the standard model. However, it is much more difficult to understand the formation of the heavier elements which are not products of stellar fusion and neutron capture reactions. Therefore, it is interesting to take a look at the chart of nuclides in figure 2.3. This chart organizes nuclides along the x-axis by the amount of neutrons and along the y-axis by the amount of protons, out to the limits of the neutron and proton drip lines. Moving away towards the drip lines, more exotic isotopes are

found. These are only created for very short periods of time in laboratories or by a violent collapse of massive stars. Exotic neutron-rich nuclei are an essential piece of the puzzle to find the balance between nucleons that form a nucleus. This is where the radioactive ion beam becomes essential again, enabling the study of these regions and providing deeper insights into the nuclear force and the various nucleosynthesis processes responsible for the creation of elements in the universe.

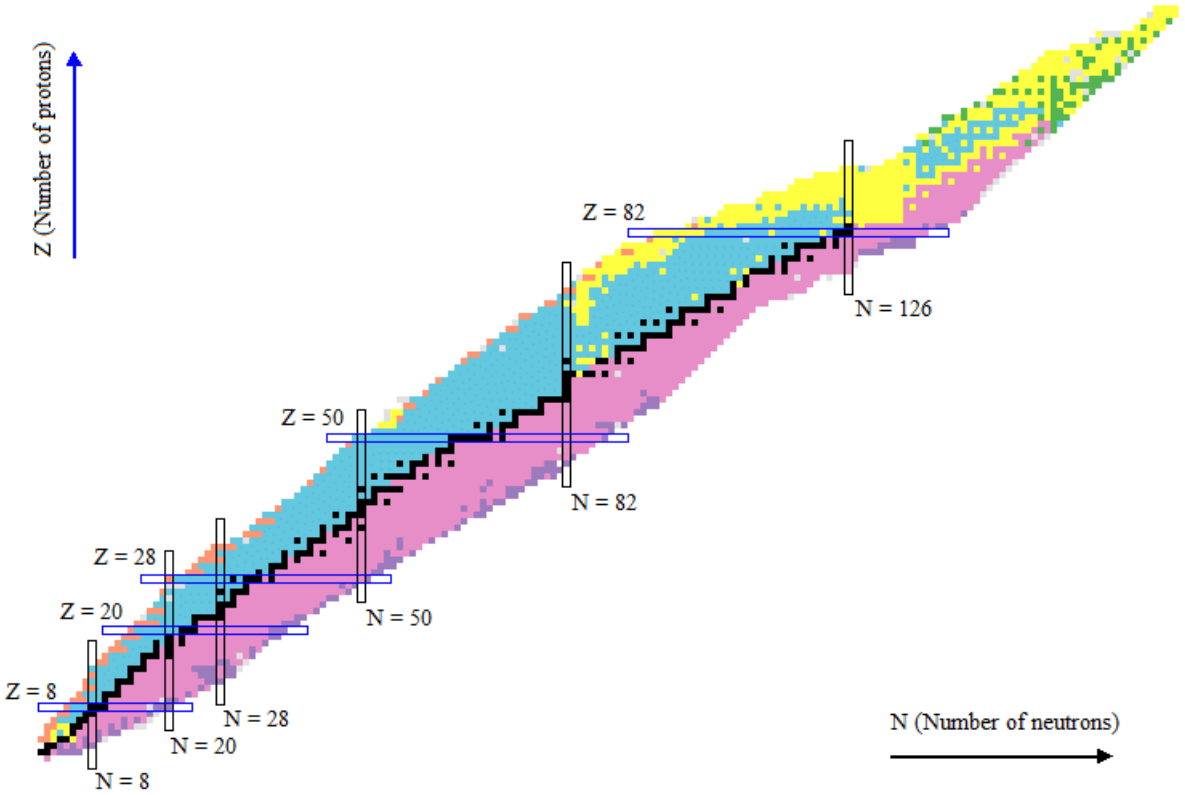

Figure 1.1: *Chart of nuclides, online taken from National Nuclear Database Center. The black blocks represent stable nuclei, the yellow blocks α decay, blue β^+/EC, and pink β^- decay.*

Many experiments are needed to get a better picture of the nuclear forces at play in these exotic nuclei. An example of this is the study of nuclear properties of neutron-rich zinc isotopes, which this dissertation aims to investigate. Chapter 2 provides an in-depth explanation of the specific interest and significance of studying neutron-rich zinc isotopes. Chapter 3 covers some theoretical background, including the various nuclear properties that can be observed from the performed experiment. The experimental approach is elaborated upon in Chapter 4, followed by a detailed description of the data analysis procedures in Chapter 5. Finally, Chapter 6 presents a discussion of the results and their implications.

Chapter 2

Physics Motivation

The study of exotic nuclei is important to understand the nuclear forces at play. Therefore, many experiments are needed to grasp the bigger picture of the existence of the nucleus. In this chapter, the importance of studying neutron-rich zinc isotopes is explained. However, first, the nuclear shell model is elaborated upon since this theoretical framework is crucial for understanding the underlying principles of studying exotic nuclei.

2.1 Nuclear Shell Model

The atomic nucleus is built out of neutrons and protons, called nucleons, which all interact with each other. A basic two-body interaction can be described by the following Hamiltonian:

$$H = \sum_{i}^{A} T_i + \sum_{i \neq j}^{A} V_{i,j}(r_i - r_j) \tag{2.1}$$

Here, three-body interactions are neglected, as many-body interactions are not analytically solvable. The exact form of the potential $V_{i,j}(r_i - r_j)$ is not known, however, it can be approximated. Therefore, two features should be taken into account [42]. First of all, a hardcore repulsion for small distances is needed ($\sim$ 0.5 fm) such that nucleons cannot overlap with each other. Secondly, there is a strong interaction between nucleons at distances of 1 fm. A good approximation for the nuclear potential is the approximation of the harmonic oscillator. This leads to a model similar to the atomic shell model that states that electrons are orbiting the nucleus at different energy levels following Pauli's exclusion principle. Using the approximation of a harmonic oscillator, magic numbers 2, 8, 20, 40, 70, and so forth are obtained. These magic numbers refer to the amount of neutrons or protons in a full shell. However, magic numbers from 40 and onward are not in agreement with experimental results. Mayer [38] and Jensen [41] proposed to add a strong spin-orbit coupling to the potential in order to obtain the magic numbers 2, 8, 20, 28, 50, 82, 126, ... that have been found experimentally. This extra factor can be written as:

$$V_{ls} = f(r)(\vec{l} \cdot \vec{s}) \tag{2.2}$$

with $\vec{l}$ the orbital angular momentum operator and $\vec{s}$ the spin operator. The effect of the spin-orbit coupling is a splitting of orbitals into j-upper (lower energy) and j-lower (higher energy) states:

$$\begin{aligned} j_> &= l + 1/2 \\ j_< &= l - 1/2 \end{aligned} \tag{2.3}$$

After the implementation of the spin-orbit coupling, shell gaps are formed due to the splitting of orbitals. The number of nucleons required to fill the shells up to these gaps is known as the magic number as can be seen in figure 2.1. A closed shell is also called a core, and the pattern of the orbits (as can be seen in figure 2.1) is known as shell structure. The block of orbits between magic numbers is called a major shell. The shell model is valid for both neutrons and protons.

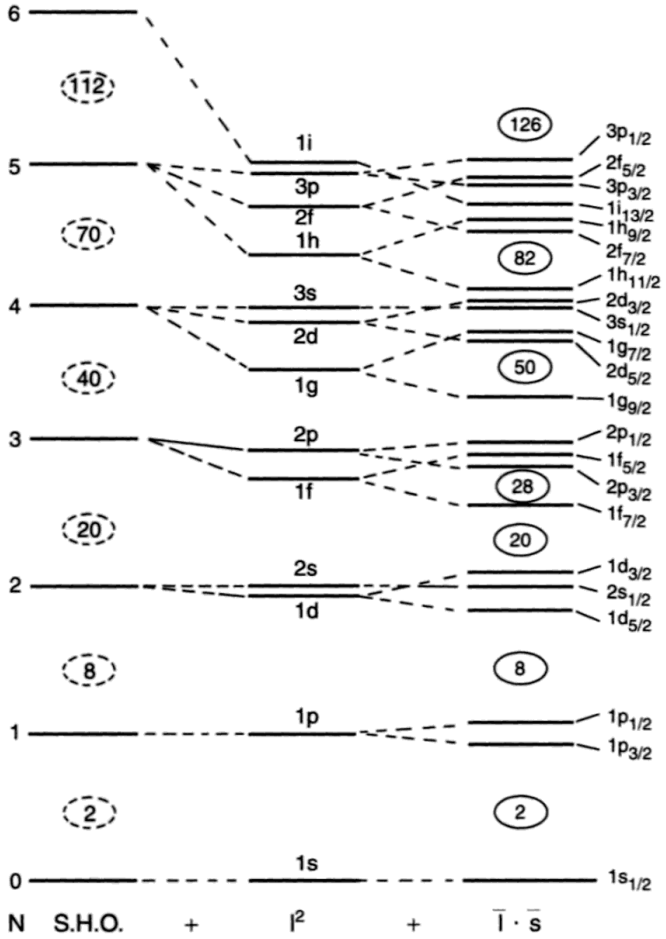

Figure 2.1: *An overview of single particle energy levels of a shell model. The left part represents the energy levels for a harmonic oscillator. By adding spin-orbit coupling to the potential, there is a splitting and lowering/rising of energy levels as illustrated on the right. Retrieved from [6].*

There are many experiments that show evidence of magic numbers, such as observed kinks in nuclear charge radii at these magic numbers. In figure 2.2 this kink can clearly be seen at N=50 and N=82 for many isotopic chains. This pattern indicates that magic nuclei are more compact than others and highlights the influence of effective interactions on nuclear structure. These results can be obtained by performing laser spectroscopy experiments.

Each nucleon possesses a spin of 1/2, and their interactions collectively determine the total spin of the nucleus. Since the degrees of freedom in nuclear shell model calculations increase drastically with the number of nucleons, the pairing of nucleons is a result of the strong pairing interaction, which provides additional binding energy. Consequently, nucleons pair to couple to spin zero, forming a closed shell, and this configuration always represents the lowest energy state in even-even nuclei. Nucleons filling a shell are considered inert as they cannot transition between single-particle states within the closed shell. Consequently, the total spin and the nuclear properties are determined by the valence nucleons.

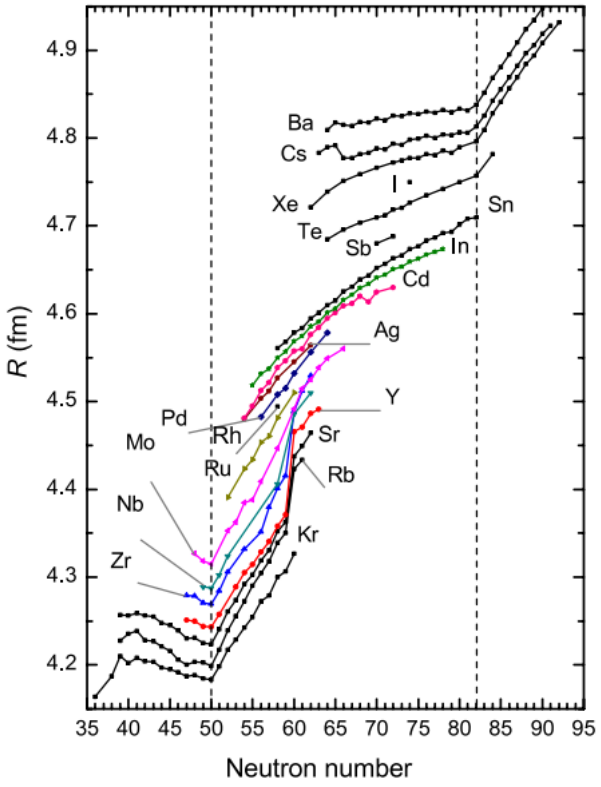

Figure 2.2: *Overview of charge radii of several isotopic chains along the neutron number, obtained from [30]. A kink can be observed at magic numbers N=50 and N=82.*

The structure of atomic nuclei is thus largely influenced by single-particle shell effects, impacting properties like binding energies and shapes. However, studying nuclei beyond the valley of stability reveals how single-particle energies change as one approaches the neutron or proton drip lines. These studies aid in making precise predictions about the limits of nuclear existence. An example of this is the rapid shift in the neutron drip line

between oxygen (Z=8, magic proton number) and fluorine (Z=9) isotopes in light nuclei. In oxygen isotopes, the neutron drip line appears at N=16, whereas in fluorine isotopes, it extends up to N=22. Understanding the evolution of shell structure from oxygen to fluorine nuclei would elucidate how the nuclear force enables the binding of six additional neutrons with the addition of a single proton, as observed in ^{31}F. The findings of M. Stanoiu et al. [18] give an estimation of the size of the N=14 and N=16 neutron gaps, resulting in the observation that ^{22}O and ^{24}O are both doubly-magic nuclei. The presence of the latter on the neutron drip line is quite unique as the drip line is very close to the stability line.

2.2 Importance of Exploring Neutron-Rich Zinc Isotopes

Magic numbers are the cornerstones of our current understanding of nuclear structure. They are well-established near the valley of stability, nevertheless, their validity is questioned in regions characterized by extreme proton-to-neutron ratios. In particular, the region with Z=28 and N=50 (doubly-magic ^{78}Ni) is of interest. Here, a breakdown of proton shell closure is predicted, leading to deformed ground states for more exotic nickel isotopes [20]. However, it is very difficult to produce ^{78}Ni with a sufficient yield to conduct measurements of the ground state properties. For this reason, experiments using other nuclei have been performed, such as the study of the ground state structure of N=51 isotope ^{81}Zn in this work. From these measurements, the moments provide insights into whether the neutrons exhibit single particle nature or a more collective behavior. The mean square charge radii contribute to the investigation of the the magic character of the N=50 gap. This is exemplified by studying the kink at this magic number, as demonstrated in the analysis of neutron-rich gallium isotopes by T.J. Procter et al [24].

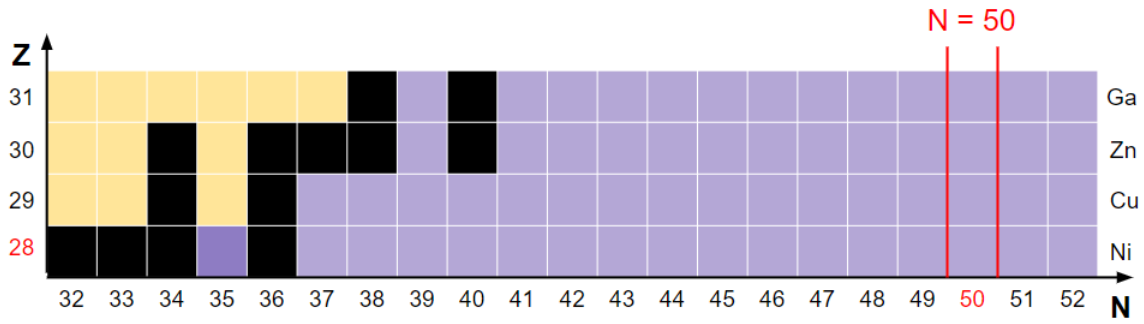

Figure 2.3: *Chart of nuclides, showing the location of the zinc isotopes. Black colored blocks represent stable isotopes, yellow blocks neutron-deficient, and purple blocks neutron-rich isotopes. In this work, zinc isotopes from N=34 till N=52 are investigated.*

The CRIS collaboration measured the hyperfine spectra of the following zinc isotopes: ^{64}Zn, ^{66}Zn, ^{67}Zn, ^{68}Zn, ^{70}Zn, ^{74}Zn, ^{75}Zn, ^{76}Zn, ^{78}Zn, ^{80}Zn, ^{81}Zn, and ^{82}Zn. Zinc has five stable isotopes: ^{64}Zn, ^{66}Zn, ^{67}Zn, ^{68}Zn and ^{70}Zn, whose locations are illustrated in the chart of nuclides (see figure 2.3). Because zinc contains 30 protons, 2 protons fill the $2p_{3/2}$ state above the magic gap of Z=28. The neutron number varies from N=34 to N=52, making it possible to investigate the magicity of N=50 as illustrated in figure 2.4.

Isotopes of zinc have already been studied in previous work by the COLLAPS group [16] [13]. Using collinear laser spectroscopy, the spin and properties of the zinc chain have been investigated from ^{64}Zn till ^{80}Zn. In this work, ^{81}Zn and ^{82}Zn are studied in addition to the work of COLLAPS, using collinear resonance ionization spectroscopy. As this technique has a high resolution, high efficiency and very low background, a comparison can be made with the data obtained from COLLAPS. Moreover, this work contains data from zinc isotopes crossing the shell gap N=50 which makes it possible to investigate its magicity by studying the nuclear charge radii and the nuclear moments. This study will be the first to explore these properties while crossing N=50, and to determine the spin of ^{81}Zn, in proximity to the doubly-magic ^{78}Ni.

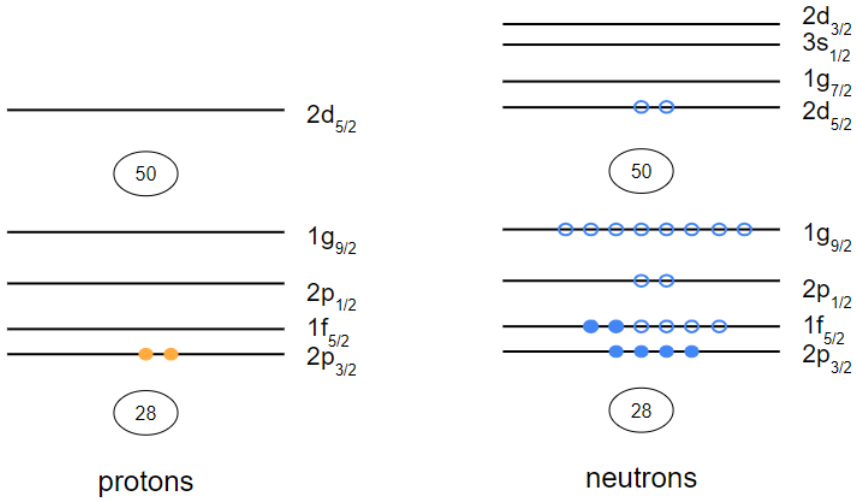

Figure 2.4: *Nuclear energy levels for protons and neutrons of zinc according to the shell model order seen in figure 2.1. In this work, isotopes from* ^{64}Zn *up to* ^{82}Zn *are investigated, filling states* $1f_{5/2}$, $2p_{1/2}$, $1g_{9/2}$, *and possibly* $2d_{5/2}$. *These isotopes are represented by the open dots.*

Chapter 3

Theory of Nuclear Observables

All isotopes are characterized by their nuclear properties, such as deformation and size. These properties can be derived from observables that can be measured during experiments. Considering the extreme single particle model, the properties of a nucleus with one neutron (or proton) outside a completely filled shell are determined by the characteristics of the orbit occupied by that neutron (or proton). It is thus essential to attain a more thorough insight on the properties of nuclei with near-magic numbers. This chapter delves into the theory of nuclear observables to provide a better understanding of how nuclear properties and shell structure are determined, following [40].

3.1 Magnetic Dipole Moment

In the classical context, the magnetic dipole moment is a consequence of charged matter (protons) rotating a center. When including quantum mechanical effects to this classical picture, the intrinsic angular moment should be taken into account. The magnetic dipole moment is mainly determined by valence nucleons, which couple to a spin I, and can be written as $\mu = gI\mu_N$. Here, $\mu_N = \frac{e\hbar}{2m_p}$ symbolizes the nuclear magneton and g the nuclear g-factor. The latter is a dimensionless factor that expresses the occupation of energy levels in the nuclear shell model. The value of μ is the expected value of the dipole moment operator projected onto the z-axis. The magnetic moment of a state with a valence nucleon in an orbit, with quantum numbers j and l, can be calculated as a function of the free-nucleon g-factors according to:

$$\mu = \begin{cases} ((j - \frac{1}{2})g_l + \frac{1}{2}g_s)\mu_N & \text{for } j = l + \frac{1}{2} \\ \frac{j}{j+1}((j + \frac{3}{2})g_l - \frac{1}{2}g_s) & \text{for } j = l - \frac{1}{2} \end{cases} \tag{3.1}$$

The free-nucleon g-factors are given by:

$$\begin{aligned} g_l^\pi &= 1, \quad g_s^\pi = 5.5857 \\ g_l^\nu &= 0, \quad g_s^\nu = -3.8261 \end{aligned} \tag{3.2}$$

After introducing these g-factors in equation 3.1, one obtains single particle moments that are called Schmidt moments:

for an odd proton:

$$\mu = \begin{cases} j - \frac{1}{2} + \mu_p & \text{for } j = l + \frac{1}{2} \\ \frac{j}{j+1}(j + \frac{3}{2} - \mu_p) & \text{for } j = l - \frac{1}{2} \end{cases} \tag{3.3}$$

for an odd neutron:

$$\mu = \begin{cases} \mu_N & \text{for } j = l + \frac{1}{2} \\ -\frac{j}{j+1}\mu_n & \text{for } j = l - \frac{1}{2} \end{cases} \tag{3.4}$$

where $\mu_p = +2.793$ and $\mu_n = -1.913$.

Nevertheless, experiments [39] show that the values of the magnetic dipole moment often lay in between these Schmidt moments. These large deviations can be attributed to two main reasons. First of all, the magnetic moments are influenced by the presence of other nucleons. This can be mitigated by introducing effective g-factors: $g_l^{eff} \sim g_l$ and $g_s^{eff} \sim 0.7 g_s$. Secondly, we are now dealing with pure single-particle wavefunctions, which in reality is often not the case for real nuclei due to configuration mixing. The g-factor can thus contain contributions from other configurations too.

3.2 Electric Quadrupole Moment

The electric quadrupole moment is the result of a more collective behavior of the nucleons. It is associated to the spherical deformation of the nucleus. The single-particle quadrupole moment of a nucleon in an orbit with spin j can be defined by:

$$Q_{s.p.} = -e_j \frac{2j-1}{2j+2} \langle r_j^2 \rangle \tag{3.5}$$

with e_j the electric charge of the nucleon and $\langle r_j^2 \rangle$ the mean square radius of the nucleon in orbit j. These two components also define the intrinsic quadrupole moment $Q_0 = -e_j \langle r_j^2 \rangle$. The spectroscopic quadrupole moment $Q_{s.p.}$ is the observed moment from experiments. If $j = 1/2$, $Q_{s.p.}$ will become zero, however, this does not mean that Q_0 is zero too. Furthermore, the charge of a neutron is zero and thus $Q_{s.p.}$ will be zero as well. To incorporate the interactions between the valence nucleons and the core, the effective charges $e_\pi^{eff} \approx 1.5e$ and $e_\nu^{eff} \approx 0.95e$ are introduced. These interactions lead to a deformation of the core. When $Q_0 < 0$, a particle in orbit j will polarize the core into an oblate deformation; when $Q_0 > 0$, a hole in orbit j will polarize the core into a prolate deformation. Furthermore, the spectroscopic quadrupole moment can be related to the intrinsic one by following relation, obtained from [40]:

$$Q_{s.p.} = \frac{3K^2 - I(I+1)}{I(I+1)(2I+3)} Q_0 \tag{3.6}$$

with K the projection of the nuclear spin I on the deformation axis. Subsequently, the intrinsic quadrupole moment can next be related to the deformation parameter β:

$$Q_0 = \frac{3}{\sqrt{5\pi}} ZR^2\beta(1 + 0.36\beta) \tag{3.7}$$

where $R = r_0A^{1/3}$, $r_0 = 1.2$ fm, and Z and A are the atomic and mass number respectively.

3.3 Nuclear Mean Square Charge Radius

One can consider the nucleus as a liquid drop. In this model, protons are distributed homogeneously over the spherical nucleus.

$$\langle r^2 \rangle = \frac{\int \rho(r) r^2 dV}{\int \rho(r) dV} \tag{3.8}$$

In the approximation of the liquid drop, the nuclear radius is related to the mass number by $R = r_0A^{1/3}$. This results into a dependency of the nuclear radius on A:

$$\langle r^2 \rangle = \frac{3}{5}R^2 = \frac{3}{5}r_0^2A^{2/3} \tag{3.9}$$

Laser spectroscopy experiments are only sensitive to experiments with changes in $\langle r^2 \rangle$ and thus the differential effect for small changes in A is given by the following relation, retrieved from [40]:

$$\delta\langle r^2 \rangle = \frac{2}{5}r_0^2A^{-1/3}\delta A \tag{3.10}$$

Deviations from the liquid drop model reveal features of nuclear structure such as shell closures, pairing and deformation.

3.4 Atomic Hyperfine Structure

Additional information about the nuclear structure can be obtained by looking at atomic effects. Atomic hyperfine structure arises from the coupling between the electronic and nuclear angular momentum (hyperfine interactions). A particular atomic orbit with angular momentum J that couples to a nuclear spin I, will give rise to a new angular momentum F according to:

$$\mathbf{F} = \mathbf{I} + \mathbf{J} \tag{3.11}$$

Thus, $| I - J | \leq F \leq I + J$ hyperfine levels are possible. The hyperfine interaction removes the degeneracy of the different F levels and produces a splitting of the electronic energy levels into $2J + 1$ or $2I + 1$ hyperfine structure levels for $J < I$ and $J > I$, respectively [40]. Hyperfine transitions follow the selection rule $\Delta F = 0, \pm 1$, and a $0 \rightarrow 0$ transition is forbidden.

Now, one can formulate a Hamiltonian representing the interaction of the nucleus with the electrons using a multipole expansion going to second order [7]:

$$H = H(E0) + H(M1) + H(E2) + ... \tag{3.12}$$

The first term represents the electric monopole, which is in fact the charge of the nucleus. This term thus represents the Coulomb force between the negative electron cloud and the positively charged point nucleus. The second term H(M1) represents the interaction of the electron cloud with the magnetic dipole moment of the nucleus, and the third term H(M2) the interaction with the electric quadrupole moment of the nucleus. Higher order terms like the magnetic octupole moment are neglected as they are largely unexplored [10] and out of the scope for this dissertation. The two last terms are thus dominating the effect of the splitting of the fine structure levels into a hyperfine structure with a magnitude of the order μeV, as can be seen in figure 3.1. These terms will be further elaborated upon.

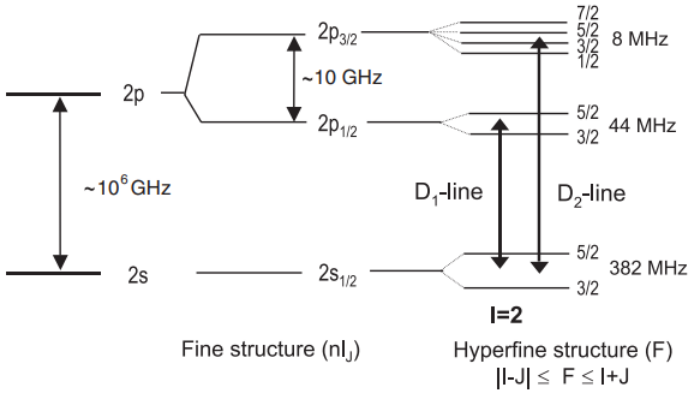

Figure 3.1: *Example of the atomic fine and hyperfine structure of* ^{8}Li*, obtained from [40].*

Magnetic dipole term

The magnetic dipole term $H(M1)$ represents the interaction between the magnetic field $\vec{B}_e$ formed by the electron cloud and the nuclear magnetic dipole moment $\vec{\mu}$:
$H(M1) = -\vec{\mu} \cdot \vec{B}_e$. The influence on the energy splitting due to this dipole term is given by:

$$\begin{aligned} \Delta E_{M1} &= -\frac{\mu B_e}{IJ}\mathbf{I}\cdot\mathbf{J} \\ &= -\frac{1}{2}\frac{\mu B_e}{IJ}(F(F+1) - I(I+1) - J(J+1)) \\ &= -\frac{1}{2}AC \end{aligned} \tag{3.13}$$

Here, the magnetic dipole interaction constant (A-parameter) is defined as:

$$A = \frac{\mu B_e}{IJ} \tag{3.14}$$

and the C-parameter is defined by the following relation:

$$C = F(F+1) - I(I+1) - J(J+1) \tag{3.15}$$

Electric quadrupole term

The electric quadrupole term further shifts the atomic energy level by an amount of:

$$\Delta E_{E2} = B\frac{\frac{3}{2}C(C+1) - I(I+1)J(J+1)}{2I(2I+1)J(2J+1)} \tag{3.16}$$

with

$$B = eQV_{zz}(0) \tag{3.17}$$

the B-parameter which captures the nuclear quadrupole moment Q and the electric field gradient (EFG) of the electrons $V_{zz}(0) = \frac{\partial^2 V}{\partial z^2}$.

3.5 Extracting Nuclear Observables

Studying radioactive isotopes and determining their nuclear moments from the hyperfine structure is possible because B_e and $V_{zz}(0)$ are usually known from experiments on the stable isotopes of the same element. Consequently, it is assumed that only the A- and B-parameters remain unknown. Nevertheless, the spin needs to be determined for highly exotic nuclei situated far from stability. This spin determination can also be obtained by the hyperfine structure measurement. Moreover, the isotope shift and thus also the differences in mean square charge radii can be obtained from these measurements. This chapter discusses how these nuclear observables are extracted from the measured hyperfine structure.

3.5.1 Magnetic Dipole Moment

From the formula for the A-parameter 3.14, it can be seen that the value for B_e needs to be determined before the magnetic moments can be extracted. However, this cannot be done with laser spectroscopy experiments. Thus, an independent experiment is needed to obtain μ. This can be done by for example nuclear magnetic resonance (NMR) on stable isotopes [40]. Using the fact that B_e is essentially a constant over the entire isotope chain, the magnetic moment of the isotope can be compared with a reference isotope from which μ_{ref} is known:

$$\mu = \frac{IA}{I_{ref}A_{ref}}\mu_{ref} \tag{3.18}$$

3.5.2 Electric Quadrupole Moment

The electric quadrupole moment can be extracted analogous to the magnetic dipole moment. The EFG $V_{zz}(0)$ cannot be determined via laser spectroscopy, but it can be obtained via nuclear quadrupole resonance (NQR). However, the quadrupole moment can be obtained by comparing the B-parameter with a reference isotope:

$$Q = \frac{B}{B_{ref}}Q_{ref} \tag{3.19}$$

3.5.3 Mean Square Charge Radius

The nuclear charge radius is an important property that enhances our understanding of both macroscopic and microscopic nuclear models. It offers valuable insights into collective nuclear behavior as explained by the liquid drop model. In addition, it also aids in the comprehension of energy level occupancy within the nuclear shell model, particularly near shell closure regions.

Isotope shift

When looking at the hyperfine structure of two different isotopes, two effects can be observed [28]. One of these is caused by the fact that isotopes have a different amount of neutrons and thus a different effective mass. The other effect is caused by the non-zero size of the nucleus, which results in a probability that electrons can enter the nucleus. These two factors will give rise to the mass shift (MS) and the field shift (FS), respectively, which leads to a total shift between reference isotope A' and isotope A:

$$\delta\nu^{A,A'} = \delta\nu_{FS}^{A,A'} + \delta\nu_{MS}^{A,A'} \tag{3.20}$$

Both principles give rise to a change in frequency of the hyperfine structure levels. The mass shift will induce a change in frequency of

$$\delta\nu_{MS}^{A,A'} = M\frac{m_A - m_{A'}}{m_A m_{A'}} \tag{3.21}$$

with M the mass shift factor [28].

The field shift reflects the change in mean square charge radii $\delta\langle r^2\rangle$, which are different for each isotope, and the effect on the electronic charge density at the nucleus. The change of frequency of the hyperfine structure can be formulated using the field shift factor F and the nuclear parameter $\Lambda^{A,A'}$:

$$\delta\nu_{FS}^{A,A'} = F\Lambda^{A,A'} \tag{3.22}$$

The field factor is proportional to the change of the electronic charge density at the nucleus during the transition. The nuclear parameter contains information about the nuclear radii and can be approximated by $\Lambda^{A,A'} = \delta\langle r^2\rangle^{A,A'}$.

King plot method

When equations 3.21 and 3.22 are substituted into the equation for the total isotope shift 3.20, the dependence on the change in mean square charge radius becomes more obvious:

$$\delta\nu^{A,A'} = M \cdot \frac{m_A - m_{A'}}{m_A m_{A'}} + F \cdot \delta\langle r^2\rangle^{A,A'} \tag{3.23}$$

The next step involves determining the values for the mass shift M and field shift F. As these two factors are assumed to be constant for an isotopic chain [3], $\delta\langle r^2\rangle^{A,A'}$ can be extracted from equation 3.23. For stable isotopes in the chain, the differences in nuclear charge radii $\delta\langle r^2\rangle^{A,A'}$ are known for a certain reference isotope A. These values are obtained from other types of experiments such as muonic experiments and can be found in

literature [27]. These known values can then be used to determine M and F by using the King plot method. After M and F are obtained from the fit, the difference in charge radii for other isotopes can be determined as well.

Dividing equation 3.23 by the reduced mass shift $\mu = \frac{m_A - m_{A'}}{m_A \cdot m_{A'}}$, gives the following equation:

$$\frac{\delta\nu^{A,A'}}{\mu} = M + F \cdot \frac{\delta < r^2 >^{A,A'}}{\mu} \tag{3.24}$$

This equation is used for fitting the two parameters M and F using the isotope shifts obtained from the experiment and the difference in charge radii from literature (all using the same reference isotope). Once the mass and field shift are determined, the nuclear charge radii of the other isotopes in the chain can be determined with respect to the reference isotope.

Chapter 4

Experimental Approach: the CRIS experiment

4.1 Isotope Mass Separator On-Line facility (ISOLDE)

The ISOLDE facility is internationally recognized for its pioneering work in producing and studying radioactive nuclei, solidifying its position as a leading laboratory in this field. ISOLDE, Isotope Separator On Line DEvice, is one of the research complexes located at CERN, and receives highly accelerated protons from the Proton Synchrotron Booster (PSB). 1.4 GeV protons are accelerated and are led to ISOLDE as high intensity pulses. These protons are needed to produce a radioactive ion beam, which is used by multiple experiments that are located in the ISOLDE facility hall. The production of this beam is further elaborated upon in this section. An overview of the main components of ISOLDE are illustrated in figure 4.1.

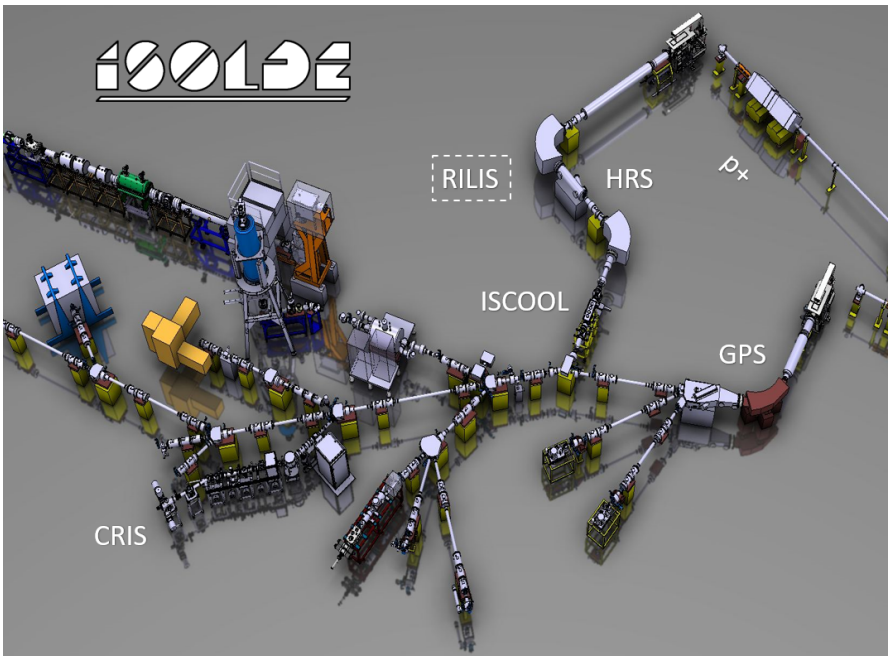

Figure 4.1: *An overview of the ISOLDE facility, obtained from [1] and adjusted.*

4.1.1 Beam Production

The first step in producing a radioactive ion beam (RIB) is the generation of radioactive nuclei. This process begins with the bombardment of a thick target by the accelerated protons from the PSB. Through different types of reactions, like spallation[1], fragmentation, and fission reactions, the desired radioactive nuclei are created. The selection of the target material depends on the specific isotopes required for the beam, taking into consideration the production yield and purity of the beam. In alignment with the focus of this dissertation, a UC_x target has been chosen. Typically, the target material is kept at an elevated temperature to facilitate the production process. In the case of uranium carbide, this temperature is set at 2000°C. Consequently, the produced exotic atoms diffuse out of the target.

Due to the substantial production of isobars through this method, it alone proves insufficient for many experiments using an ion beam. For numerous users of ISOLDE, it is essential for the beam to contain a high degree of chemical purity. Hence, a separation between nuclides with differing proton numbers (Z) becomes necessary. The Resonance Ionization Laser Ion Source (RILIS) addresses this need through a technique grounded in atomic physics known as step-wise resonance photo-ionization. By exploiting the unique electronic structure of different atomic species, RILIS executes the ionization process, which is highly Z-selective. This process involves initially exciting the atoms to a state that is characteristic for the element of interest. As a consequence, only these atoms will be ionized by a second laser, generating the wanted radioactive ion beam. Following this, the beam is typically accelerated to 60 keV and directed towards the High Resolution Separator (HRS) for mass separation. The HRS comprises two bending magnets designed to separate the ion beam based on mass. The combination of the HRS's ability to isolate specific isobars and the element-selective ionization provided by RILIS enables us to conduct precise measurements.

4.1.2 ISCOOL

Before the radioactive ion beam reaches the CRIS setup, the experimental setup used in this dissertation, the beam needs to be cooled. In addition, a bunched beam is required and thus not a continuous one as was described up until now. For these purposes, the ISolde COOLer (ISCOOL) is used to manipulate the radioactive ion beam to comply with the experimental requirements in order to improve the optics of the ISOLDE beam line. ISCOOL cools the incoming beam through collisions with a buffer gas inside which leads to a loss of kinetic energy. Helium is an excellent gas to use, as it is highly chemically stable and it has a very low mass, which slows down the heavier ions. Concerning the beam confinement, a linear Paul trap is able to confine the beam along the radial direction. Quadrupole electrodes, which are aligned along the beam axis, are connected to an oscillating RF field. In order to confine the isotope of interest, the RF field parameters can be adjusted. This also leads to a disposal of impurities out of the trap.

[1]Spallation is a violent reaction in which a target is bombarded by very high-energy particles. The incident particle, in this case a proton, disintegrates the nucleus through inelastic nuclear reactions, resulting in the emission of protons, neutrons, α-particles, and other particles.

Once the beam is cooled, it has to be bunched, if required, and then accelerated once more to 60 keV and transported to the experiment. The bunching process utilizes axial electrodes, which define a potential profile, to perform a push-and-pull method [2]. This bunching is vital for e.g. the CRIS setup, as a minimal time dispersion is required. The bunching method involves elevating the voltage of one of the axial electrodes while lowering the voltage of the extraction plate simultaneously as illustrated in figure 4.2. In other words, the ions are first confined in a potential well, and are then released in bunches by dropping this potential.

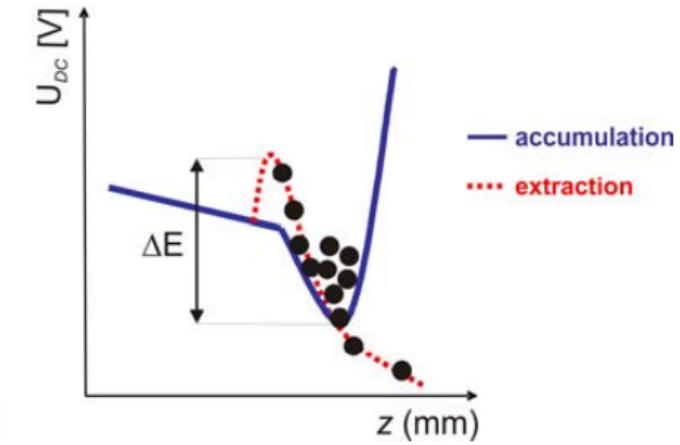

Figure 4.2: *Push-and-pull method for bunching the ion beam. Figure obtained from [2].*

Now, the bunched beam needs to be accelerated once more towards the experimental setup. Using an accelerated beam is necessary to overcome Doppler broadening of the hyperfine peaks. Furthermore, a high resolution is required as hyperfine splitting is of the order of μeV and a spread in velocity can broaden the peaks of the spectrum as can be seen from:

$$\delta E = mv \cdot \delta v \tag{4.1}$$

Here, δE is the spread in kinetic energy which is constant during the acceleration. When the beam is accelerated, the speed will increase and thus the spread in velocity must decrease. Doppler broadening can thus almost be neglected, and the final resolution is dominated by a combination of the linewidth of the laser and the natural linewidth.

4.2 Collinear Resonance Ionization Spectroscopy

Once the radioactive ion beam is obtained, as discussed in the previous section, the beam can be guided to different experimental setups. The experiment studied in this dissertation makes use of CRIS, short for Collinear Resonance Ionization Spectroscopy. A technical drawing of this setup is shown in figure 4.3. First the beam is guided to the charge exchange cell (CEC) where the ions within the beam are neutralized. This neutralization occurs due to electron transfers between an alkali metal vapor within the CEC and the ion beam. The alkali metal is placed in the CEC, which is then heated up to 150°C. To create high vacuum conditions, the CEC is pumped down to 10^{-6} mbar. The

ions that did not get neutralized are ejected from the beam by a deflector located behind the CEC as is depicted in figure 4.4.

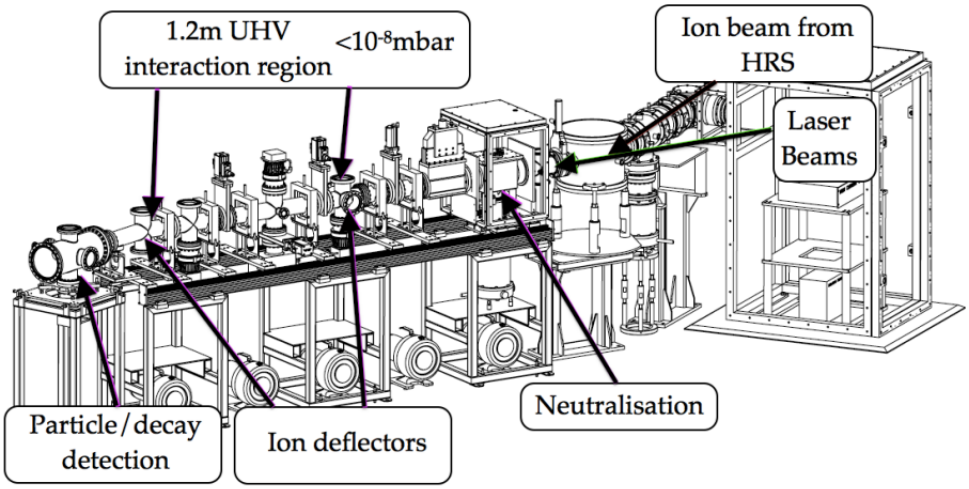

Figure 4.3: *Scheme of the CRIS setup, taken from [23].*

Now, the atom beam enters the interaction region and the resonance ionization can be induced. Due to overlapping laser pulses (in space and in time), the atoms in the atom bunch can be ionized through a step-wise process. The principle behind collinear resonance ionization spectroscopy is to scan over the frequency of the excitation laser, and if it hits resonance of the hyperfine spectrum, the atoms will be ionized by the ionization laser. To limit the background, the interaction region is held at an ultra high vacuum as well, with a pressure below 10^{-8} mbar. In this way, less off-resonance ionizations can occur from collisions with other molecules or atoms in the beam line.

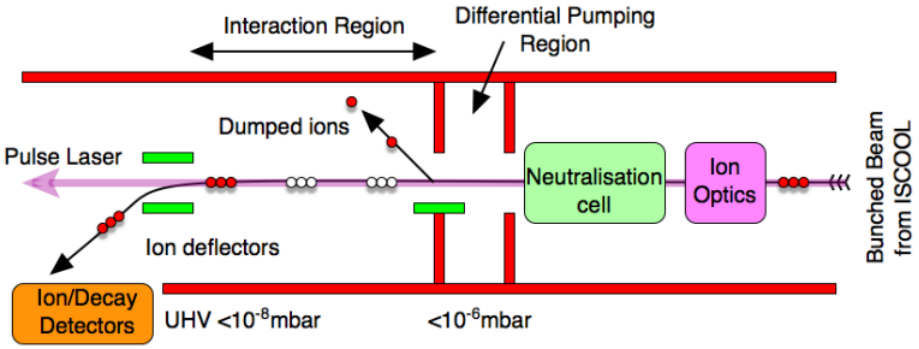

Figure 4.4: *Scheme of all different steps within the CRIS setup. The bunched ion beam from ISCOOL arrives at the right. The outgoing in-resonant ion beam is led to the detectors by ion deflectors as can be seen on the right. Figure obtained from [23].*

After the interaction region, the ion bunch is guided towards the detection region by ion deflectors. The ion bunch is focused onto a copper dynode - held at a negative voltage - which leads to a production of secondary electrons. These electrons are subsequently

detected by a MagneToF, and the signal is then processed with a time digitizer with sub-ns resolution. The hyperfine spectrum is thus reconstructed by counting the ion rate as a function of the laser frequency. Ensuring that the experiment runs smoothly, a Quantum Composers pulse generator is utilized to generate the master trigger, controlling the pulsed lasers, gating detection time and releasing ions from ISCOOL [23].

4.3 Ionization Scheme

This experiment uses a three-step ionization process for studying the $3P_2 \rightarrow 3S_1$ transition as shown in figure 4.5. First, the $4s4p\ ^3P$ groundstate of zinc is excited to the $4s5p\ ^3S$ state, a 481.1 nm transition. This excitation is performed with an injection seeded Ti:Sa laser, which is a pulsed narrow band laser of 20 MHz. The next step is another excitation step to the $4s6p\ ^3P$ state with a 692 nm transition. A pulsed dye laser (PDL) is used to do so, which is a broadband laser of 10 GHz. Lastly, the ionization step is performed by a 1064 nm Litron laser, a high power broadband laser. This is the non-resonant step which ionizes the atom by exciting the atom above the ionization potential (IP). The ISCOOL bunch rate is synchronized to this frequency to ensure precise spatial and temporal overlap between the laser beams and atom bunches. Nevertheless, the ionization laser fires immediately after the excitation laser to minimize the AC Stark effect. This adjustment is crucial for preventing peak broadening to the point where no hyperfine structure can be extracted anymore [7].

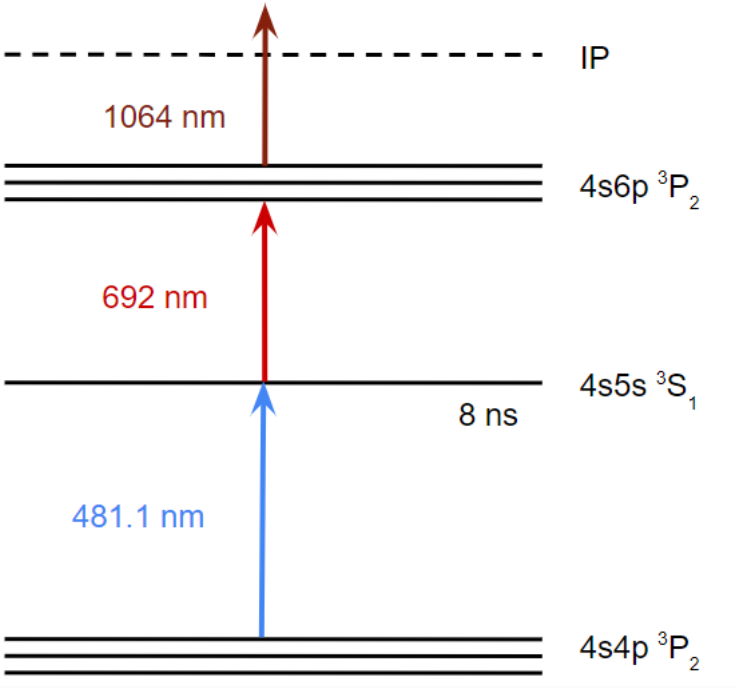

Figure 4.5: *Three-step ionization scheme used in this experiment.*

Chapter 5

Analysis

Prior to presenting the results, a detailed overview of each step in the process of analyzing and fitting the spectra will be provided. Firstly, the analysis of the raw data leading to the spectrum will be discussed, followed by a description of the fitting procedures. These form the foundation of the analytical process. Additionally, the reference isotope ^{70}Zn is analyzed, thereby investigating the stability of centroids for calculating the isotope shifts. This investigation aims to verify the reliability of the experimental setup and lays the groundwork for subsequent discussions on results and interpretations.

5.1 Data Acquisition

The CRIS experiment utilizes two data acquisition systems to manage its operations effectively. The first one is CRISTAL (CRIS laser Tuning, Acquisition and Logging) and functions as the control center for the laser system and the counting of MagneToF events. This data aggregation enables real-time visualization during acquisition. The second system is an acquisition module with onboard digital pulse processing algorithms and records the data event by event, from which correlations in time or between detectors can be reconstructed offline [22]. The data of each scan is stored in different files, containing information about the laser wavenumber, CEC voltage, ISCOOL voltage, and the observed events.

In the performed experiment, the hyperfine structures of zinc isotopes going from $N = 34$ to $N = 52$ are measured. There are multiple scans per isotope, which makes it possible to take weighted averages of the fitting parameters resulting in a better precision. Furthermore, a reference isotope is chosen, which is stable and easy to measure. This reference isotope is necessary for the data analysis to register long-term drifts in the laser frequency measurement (e.g. due to drifts in the wavemeter readout), safeguarding the quality of the analysis. In this run, ^{70}Zn is chosen as the reference isotope as it satisfies all requirements. This isotope is used at the start of the experiment to optimize the beam. It is also employed to synchronize the timing of the lasers, ensuring they overlap in space and time with the atom beam.

The first step of processing the obtained data is to filter out bad scans, which are not usable due to e.g. a laser losing lock. Furthermore, scans that were merely used for optimizing the ionization efficiency can also be filtered out. These scans are mainly very

scattered scans and do not contain valuable information for further analysis and are thus discarded. For this reason, the first scans of the reference isotope are considered as unsuitable and are also discarded. Furthermore, it is possible that the data should be cut for the same reasons as still valuable information can be retrieved from it.

5.2 Fitting Procedure

Each scan consists of multiple data files, each giving information about the major instruments. The 'wavemeter'-file contains readouts of the wavemeters, among which the wavenumber of the scanning laser and of the reference diode laser. The 'tagger'-file includes the observed events by the detector and the time since the bunch was released by the ISCOOL cooler buncher. Furthermore, the 'ISCOOL voltage'- and the 'CEC voltage'-files contain the values of the voltage at each timestamp which was used at ISCOOL and the CEC to accelerate the bunch. An important note is that each of these files contain the timestamp of each bunch, accompanied with the relevant data of that file. The information from these two files are needed to account for the Doppler shifting of the laser frequency when the atoms are in the interaction region of the CRIS setup. So, in order to derive the frequency in the rest frame from the laboratory frame's frequency, the following equation is used:

$$\nu_{rest} = \nu_{lab}\sqrt{\frac{1-\beta}{1+\beta}} \tag{5.1}$$

with

$$\beta = \sqrt{1 - \frac{m^2c^4}{(eV + mc^2)^2}} \tag{5.2}$$

where m is the mass of the nucleus and V is the ISCOOL and CEC voltage at which it was accelerated. This correction is essential for ensuring a reliable isotope shift due to the mass dependency outlined in equation 5.1. The acceleration experienced by ions of a specific isotope upon exiting ISCOOL should ideally remain constant for a laser scan. However, the ISCOOL voltage fluctuates slightly as can be seen in Appendix A.1, figure A.1. From histogram A.2, a Gaussian fit can be determined, resulting in the mean voltage of ISCOOL with its standard deviation: 29929.94 ± 0.45 V. This voltage fluctuation is thus negligible, however, larger fluctuations at different timestamps are observed and a correction is thus necessary. In addition, each data point undergoes individual correction during the Doppler shifting process as the CEC voltage changes when a voltage scan is performed.

Before the fitting of the spectra can be performed, the data of each scan needs to be binned first. This improves the signal-to-noise ratio by averaging or consolidating data points within each bin. In addition, binning helps to simplify the complex dataset by aggregating data points into meaningful groups or intervals. This reduction in complexity makes it easier to analyze and interpret the data. There are two types of scans, namely voltage scans and laser scans. A laser scan involves directly scanning the laser frequency to cover the hyperfine structure. This method, while straightforward in its approach, often faces challenges in maintaining laser stability during the scan. The feedback loop necessary for precise wavelength control can also result in slower operation. In contrast, a voltage scan modifies the speed of the atoms by varying the voltage applied to the CEC

electrodes. This change in speed induces a frequency shift through the Doppler effect, allowing the atoms to interact with a fixed-frequency narrowband laser. This method offers significant advantages in terms of stability, as the laser frequency remains constant, minimizing power fluctuations. Additionally, the electronics used for voltage adjustments typically respond faster than the laser frequency control systems, making voltage scans more time efficient for experiments with high production rates (on the order of $\sim 10^3$ ions per second [36]).

These two types of scans require a different method of binning. An example of the result of this procedure can be seen in figure 5.1 for the reference isotope. A binsize of 20 MHz is chosen during the analysis performed in this dissertation.

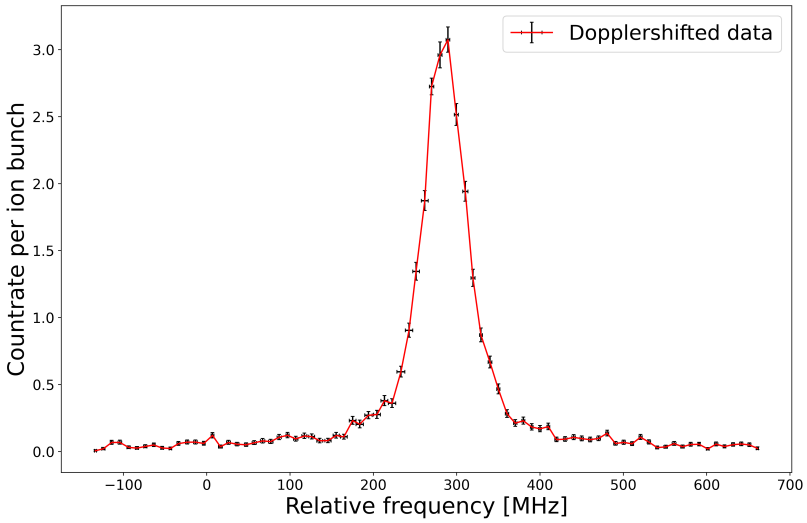

Figure 5.1: *Result of Doppler shifting scan 5466 of the reference isotope* ^{70}Zn.

Binning a voltage scan

For a voltage scan, the bins are first initialized with a certain size which can be varied. A small binsize induces more details in the hyperfine spectra. However, for low count rates, this can give rise to increasing statistical errors. Besides, a larger binsize provides a more averaged spectrum, smoothing out details. The optimal choice of binsize depends on several factors, including the count rate, the width of the hyperfine peaks, and the potential overlap of these peaks. The next step is to group the data by voltage. In this manner, data points falling within the same voltage range are grouped within this bin. After the binning, the data is Doppler shifted. Next, within each bin, the frequency and its associated error are converted into MHz and transformed into a relative frequency with respect to the transition frequency. The number of bunches present in each bin is calculated by counting the amount of unique bunch numbers in each bin. The counts per bin are calculated and an error is assigned following Poisson statistics. The binned data is then sorted with respect to the frequency.

Binning a laser scan

The first step to analyze a laser scan, also called frequency scan, is to Doppler shift the data. Afterwards, the initialization of the bins is performed analogous to explained the voltage scan. Then, the data is grouped in each bin by laser frequency in the atom frame. Following that, the procedure is the same as the voltage scan. Within each bin, the frequency and its associated error are converted into MHz and transformed into a relative frequency with respect to the transition frequency. The bunches are calculated by counting the amount of unique bunch numbers in each bin. The observed events per bin are determined and the error is assigned following Poisson statistics. The binned data is then sorted with respect to the frequency.

Fitting with SATLAS2

The analysis of the hyperfine spectra is executed using the Python fitting package SATLAS2. This package is created by Wouter Gins and Bram van den Borne [45]. In order to be able to fit the data, the following fixed values should first be given as input:

- Nuclear spin I
- Angular momentum J of the lower and upper states of the transition

In addition, initial guesses for the following output parameters can be given as well:

- A and B hyperfine parameters of the lower and upper states of the transition
- Full Width at Half Maximum (FWHM) of the chosen lineshape
- Centroid of the hyperfine spectrum
- Background count rate
- Scale of peak amplitudes

The output of the code is a plot of the fit, an example of which can be seen in figure 5.2. The fit parameters are also listed together with their uncertainties based on a 68% confidence interval (1σ). To evaluate the goodness-of-fit, a reduced χ^2-value is attributed. A few scans had a χ^2_ν-value higher than 20, although the fit seems to follow the data good. This larger χ^2_ν-value can be explained by the very small error bars on the Doppler shifted data. Since these scans experience a high amount of counts per bunch, the statistics are very high as well, leading to small error bars. For this reason, the uncertainties of the fit parameters are scaled by multiplying them by the square root of the χ^2_ν-value of that fit.

5.3 Reference Isotope Analysis

As already mentioned before, a reference isotope is chosen which is scanned multiple times during the experiment. This is done to register the stability of the measured laser frequencies and to calculate the isotope shifts. ^{70}Zn is chosen as the reference isotope, containing 40 neutrons and 30 protons (an even-even isotope), and it has a nuclear spin $I = 0$. A zero-spin means that only one hyperfine peak is present. The centroids of the

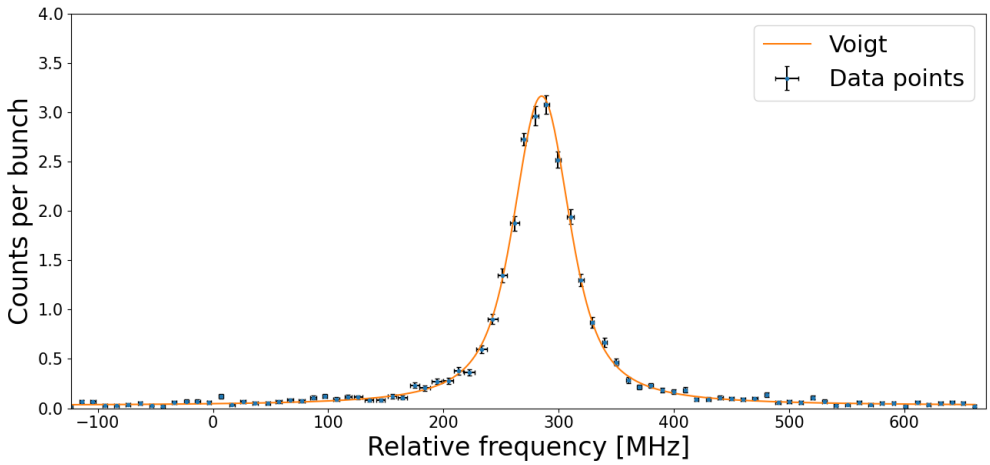

Figure 5.2: *Result of fitting with SATLAS2 of scan 5466 of the reference isotope* ^{70}Zn.

fitted spectra for ^{70}Zn are observed to look for possible variations, which can be indications of systematic errors. These variations and other characteristics of the fit are further investigated in this part.

A first step of investigating the fit characteristics for the reference isotope is to assign a lineshape to fit the hyperfine spectrum. For the reference isotope a Voigt lineshape is chosen. A Voigt is a probability distribution resulting from the convolution of a Lorentzian and a Gaussian profile. The Gaussian part of the lineshape mainly results from Doppler broadening. However, this contribution is usually only minor due to the small velocity spread of accelerated beams. The other broadening mechanism is due to power broadening and due to the natural linewidth, which has a Lorentzian shape. Therefore, the FWHM of these two contributions is given as an initial guess. In figure 5.3, a comparison is made between the different lineshapes for the reference isotope. Based on this comparison, it is evident that adopting the Voigt profile is the appropriate choice. An average FWHM for the Gaussian contribution is found to be 31 MHz and for the Lorentzian contribution 40 MHz.

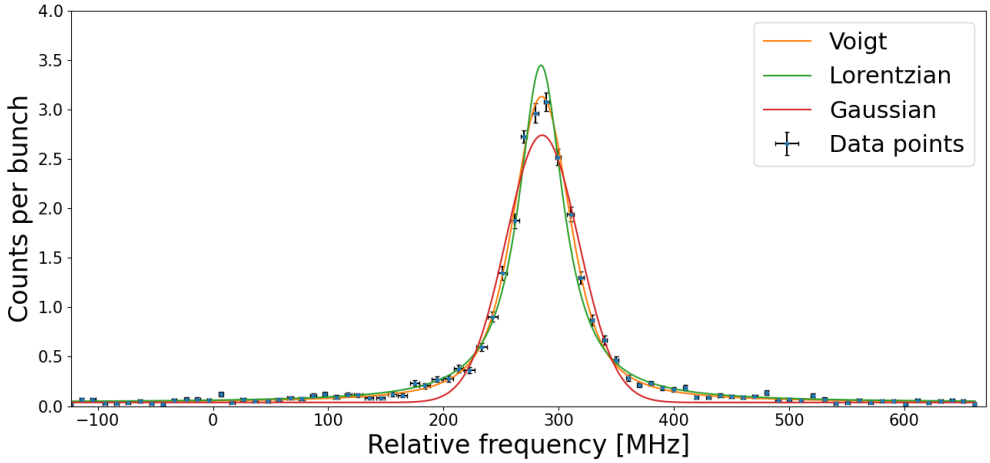

Figure 5.3: *Comparison of a Voigt, Lorentzian, and a Gaussian lineshape of scan 5466 of the reference isotope* ^{70}Zn.

In order to investigate the isotope shifts, first, the variation of centroids over time is analyzed for the reference isotope. The accuracy of the isotope shift strongly relies on the stability of the wavemeter readout. For this reason the diode wavenumber is examined as well. The diode laser is typically very stable, maintaining an almost constant frequency over time. Therefore, if the wavemeter readout indicates significant variations in the diode wavenumber, these fluctuations are likely due to drifts in the wavemeter readout itself. This assumption allows us to consider that the drift is consistent across all wavemeter channels and thus a correction is applied to the scanned laser frequency. In Appendix A.2, figure A.3, an overview of the diode wavenumbers of all reference scans over time is illustrated. From histogram A.4 a Gaussian fit is determined, resulting in the mean diode wavenumber with its standard deviation: 12578.848965(35) cm^{-1}. We can therefore conclude that the fluctuations are minimal, indicating that the wavemeter readout remains stable throughout the experiment. Nonetheless, a correction is still applied during the Doppler shifting of the data.

The wavemeter stability can also be concluded from the centroids of the reference isotope ^{70}Zn over time, as can be seen in figure 5.4. A weighted mean is taken of all centroids which is the reference centroid used for the calculation of the isotope shifts. To determine the error of the mean centroid, a histogram is made to look for a Gaussian behavior, as there are many reference scans. From this histogram, the error of the centroid can be determined from a Gaussian fit, namely the standard deviation (1σ), as can be seen in figure 5.5. The reference centroid is fixed for the calculation of the isotope shifts at 283.4 ± 2.6 MHz.

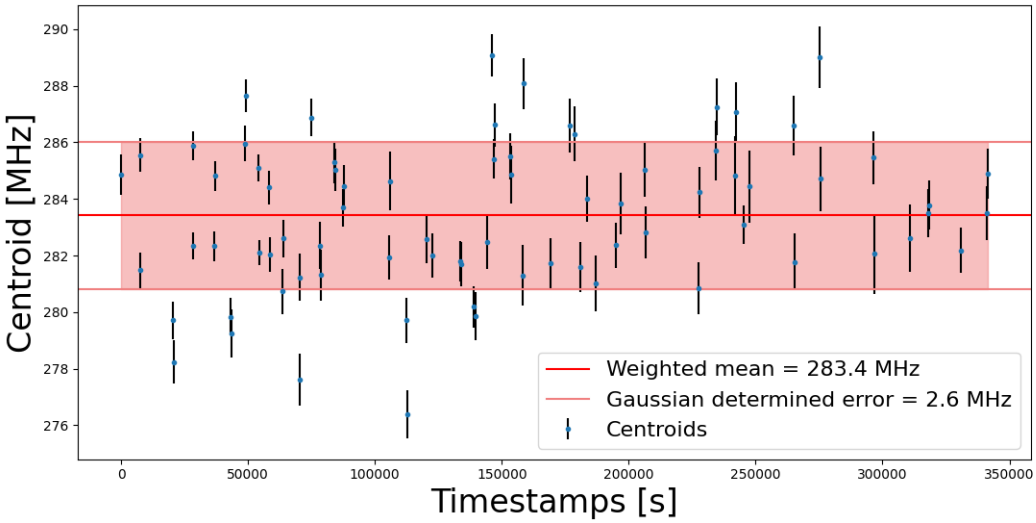

Figure 5.4: *Overview of all reference centroids over the duration of the experiment.*

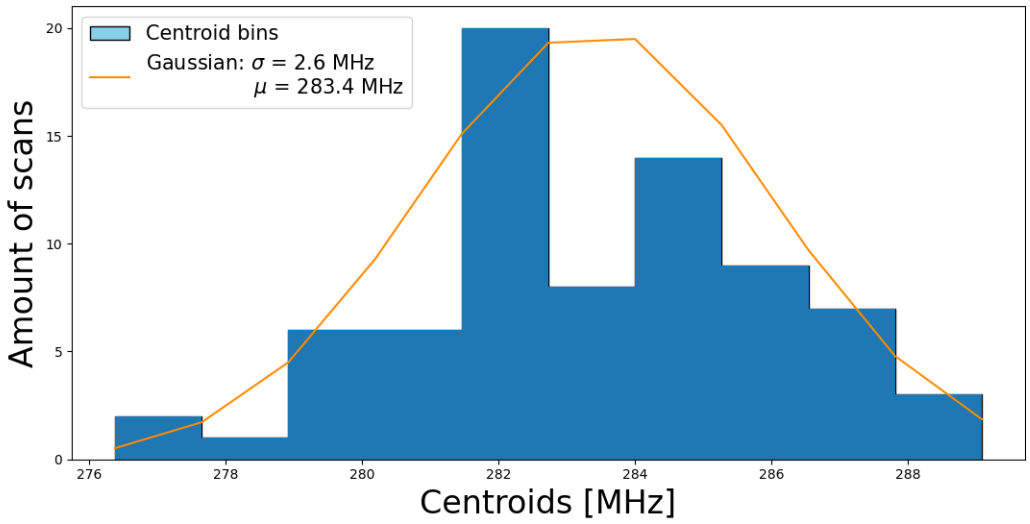

Figure 5.5: *Gaussian fit of the centroid histogram.*

Chapter 6

Results and Discussion

6.1 Spin Assignment and Nuclear Moments of ^{81}Zn

Looking at the energy levels of $N = 51$ isotones, which have one neutron above the $N = 50$ shell closure, provides valuable insights into their nuclear structure. The ground state of these N=51 isotones is expected to have a neutron in the $d_{5/2}$ orbit with a spin/parity of $5/2^+$, illustrated in figure 6.1. The first excited state is found to be $1/2^+$, due to a neutron in the $s_{1/2}$ orbital. As can be seen in 6.1, a drop in energy of the excited state $1/2^+$ is experimentally observed from $Z = 40$ down to $Z = 32$. The difference in energy between this excited state and the $5/2^+$ ground state changes due to the effect of the central and tensor components of the monopole interaction on the $d_{5/2}$ orbit within the shell model framework [15]. Since the central force is always attractive and it is more strongly for orbits with higher angular momentum, removing protons from any orbit results in a less bound $\nu d_{5/2}$ level. Thus along the isotone chain from ^{91}Zr to ^{79}Ni, the $\nu d_{5/2}$ moves closer to the $\nu s_{1/2}$ state due to the central force. Furthermore, the tensor force is attractive between $j_<$ and $j'_>$ and is repulsive between $j_>$ and $j'_>$ states. As $\nu d_{5/2}$ is a $j_>$ state, the tensor force is repulsive for protons filling the $\pi p_{3/2}$ ($j'_>$) state and attractive for protons filling the $\pi f_{5/2}$ and $\pi p_{1/2}$ ($j'_<$) states. The tensor force thus results in a less bound $d_{5/2}$ state from ^{83}Ge onward, moving closer to the $s_{1/2}$ state. Shell model calculations using jj45pna [31] predict that the $1/2^+$ level becomes the ground state in ^{81}Zn and be more or less degenerate with the $5/2^+$ level [35]. Ab-initio calculations [29] are performed only for ^{79}Ni and also predict an inversion of the $s_{1/2}$ and $d_{5/2}$ states. It is thus clear that an experimental spin assignment for ^{81}Zn is necessary.

The spin assignment is based on fitting the hyperfine spectrum of ^{81}Zn. The goodness of the fit and the ratio of A-parameters are good measures for the spin. The goodness of the fit is determined by χ^2_ν and the ratio of A-parameters should be constant over the whole isotopic chain, thus deviations result in a wrong spin assignment. For this reason, the fit of ^{75}Zn is used to determine this ratio of A-parameters as its spin is well-known. From the output of the fit parameters, the ratio of A-parameters $= \frac{A_u}{A_l}$ is set to 2.382 ± 0.002. From the J-values of the $3P_2 \rightarrow 3S_1$ transition and the possible spin value, the amount of peaks in the hyperfine spectrum can be determined as already explained in chapter 3.4. By plotting the hyperfine spectrum, the amount of peaks that can be seen is eight, however, one of these peaks is expected to be a doublet and thus there are likely nine peaks possible in total. A spin of 1/2 can be ruled out as from this spin, only three peaks

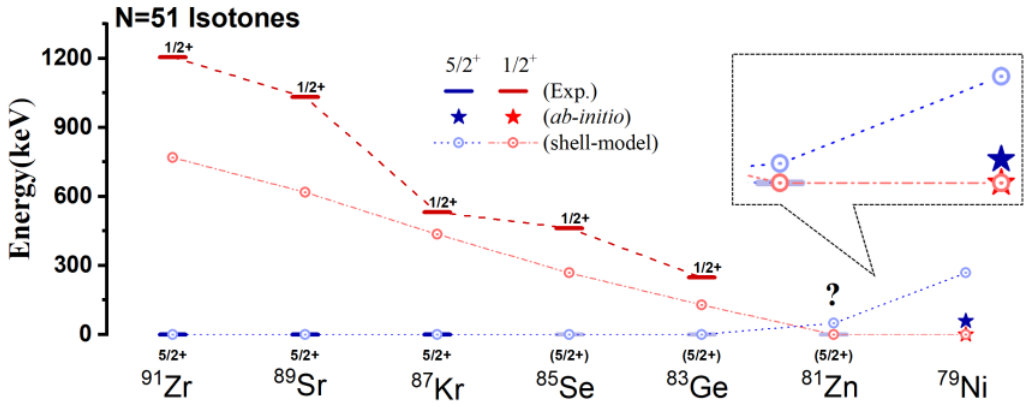

Figure 6.1: *Comparison of the* $1/2^+$ *and the* $5/2^+$ *energy levels from experiments and theoretical calculations along the N=51 isotone chain. Figure taken from [35].*

should form the hyperfine spectrum. The remaining possible spins are 3/2, 5/2 and 7/2. In figure 6.2, the fits of spin 3/2 and spin 7/2 are shown. It is clear that both fits do not fit the data as some of the observed peaks in the spectrum cannot be fit. This becomes evident upon examining the baseline beneath the plotted data points. Note that spin 3/2 does not fit the last two peaks at all, and spin 7/2 does not fit the first two peaks.

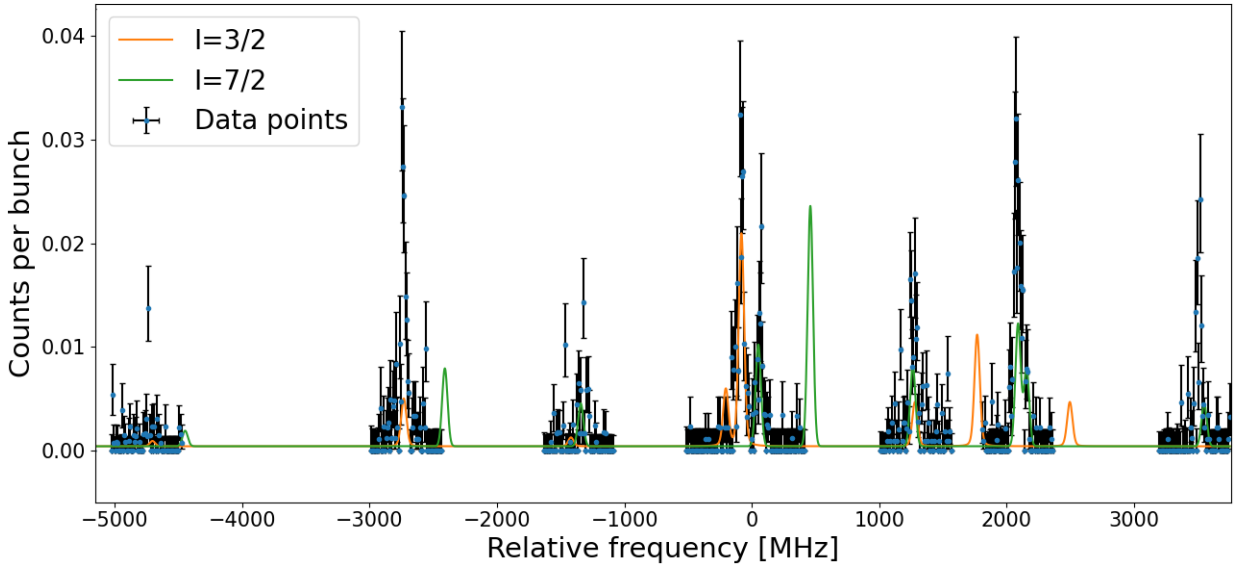

Figure 6.2: *Plot of the fits for a spin assignment of* 3/2 *and* 7/2 *for the ground state of* ^{81}Zn. *These fits clearly do not fit the data: spin* 3/2 *does not fit the last two peaks at all, and spin* 7/2 *does not fit the first two peaks.*

When assigning a spin of 5/2 as the ground state of ^{81}Zn, a good fit with $\chi^2_\nu = 0.53$ is obtained which is shown in figure 6.3. The fit results are the following:

- $A_l = -577.74 \pm 1.20$ MHz
- $B_l = -79.78 \pm 8.73$ MHz
- $A_u = -1375.05 \pm 1.99$ MHz
- $B_u = 0$ MHz

These parameters are used to extract the nuclear moments. Since B_u is zero, B_l is chosen to extract the quadrupole moment and A_l to extract the magnetic moment.

Moreover, a ratio of A-parameters of 2.380 ± 0.006 (compared to the ratio of A-parameters of ^{75}Zn: 2.382 ± 0.002) demonstrates that spin 5/2 can be assigned to the ^{81}Zn ground state. Another way to confirm the proposed spin for the isotope with a single unpaired neutron above N=50, is to compare the experimental g-factor with that of a neutron in the $d_{5/2}$ orbit. Therefore, the magnetic moment needs to be extracted from the fit result of the hyperfine A-parameter of ^{81}Zn.

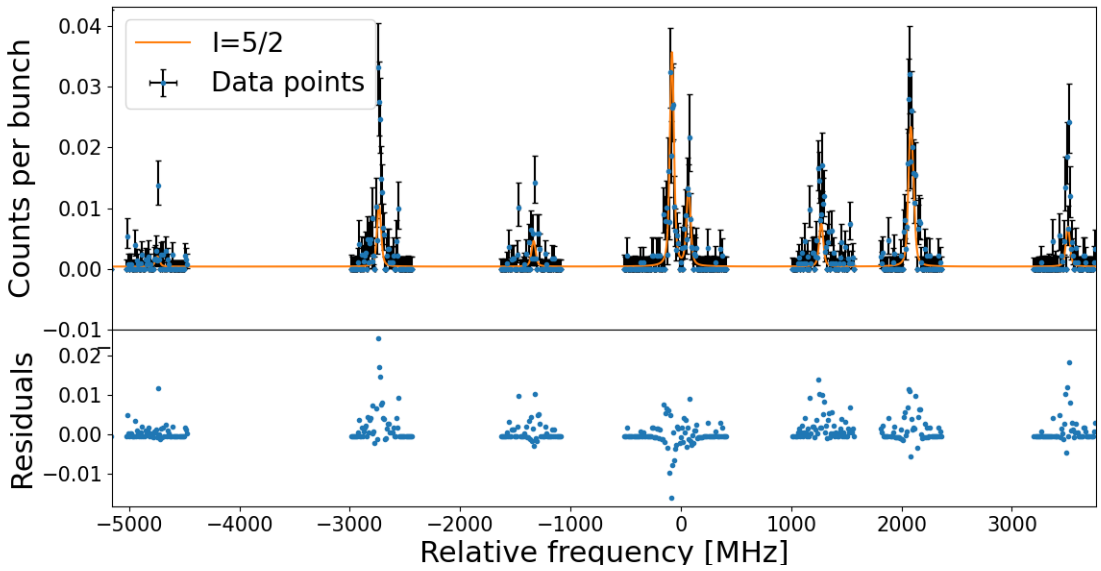

Figure 6.3: *Plot of the fit for a spin* 5/2 *with* $\chi^2_\nu = 0.53$.

The dependence of the spin on the nuclear moment necessitates a reference isotope with a well-known magnetic moment and spin, as expressed in equation 3.18. ^{67}Zn is chosen as this reference, with spin $I_{ref} = 5/2$, $A_{ref} = 531.2 \pm 1.1$ MHz, and magnetic moment[2] $\mu = 0.875479 \pm 0.000009\ \mu_N$. Due to a too fast laser scan of ^{67}Zn, fitting its hyperfine spectrum to obtain A_{ref} was not possible. For this reason, A_{ref} is taken from COLLAPS [13] as the values of the A-parameters agree within error bars, validated by the fit output from ^{75}Zn of this work. The results of this approximated method are the following magnetic moment and g-factor for ^{81}Zn:

$$\mu = (-0.9522 \pm 0.0028) \cdot \mu_N$$

$$g = -0.3809 \pm 0.0011$$

Now, this g-factor can be compared to the effective single particle g-factor for a neutron in the $2d_{5/2}$ orbit, which is a correction of the free g-factor ($g_{SP} = 0.7 g_{free}$) as explained in chapter 3.1. In figure 6.4, an overview of g-factors obtained by COLLAPS [13] with the addition of the g-factor of ^{81}Zn of this work is presented. A small deviation from the

[2]The magnetic moment of ^{67}Zn is obtained from [43].

single particle g-factor ($2d_{5/2}$) is observed which is the expected ground state from the spin assignment. Note that the g-factor of ^{81}Zn is closer to the value of the single particle g-factor of the $1g_{9/2}$ state. Since all states below the N=50 shell closure are occupied, the $1g_{9/2}$ state is already completely filled. In order to have the $1g_{9/2}$ state as the ground state configuration of ^{81}Zn, a neutron excitation across the N=50 shell gap is required, leading to a particle-hole excitation as the ground state. The assumed spin of ^{81}Zn, namely 5/2, can indeed be obtained by the coupling of $1g_{9/2}^{-1}$ to $(\nu d_{5/2}^2)_{2^+}$, and $(\pi f_{5/2}^2)_{2^+}$ from the two protons above the Z=28 gap. However, further investigation is necessary to compare the magnetic moments of these configurations with the one obtained from the experiment. In addition, these magnetic moments can be compared to shell model [33] and ab-initio [44] calculations along the N=51 isotone chain.

Besides, a comparison with the Schmidt value is made along this isotone chain, presented in figure 6.5. The data for the magnetic moments of ^{87}Kr, ^{89}Sr, and ^{91}Zr are taken from [17], [26], and [8] respectively. A large deviation from the Schmidt value is seen for the magnetic moment of ^{81}Zn which points to a non-single particle like behavior. The importance of theoretical models allowing configuration mixing is highlighted once more, indicating that additional research is required to further investigate the nuclear moment of different configurations.

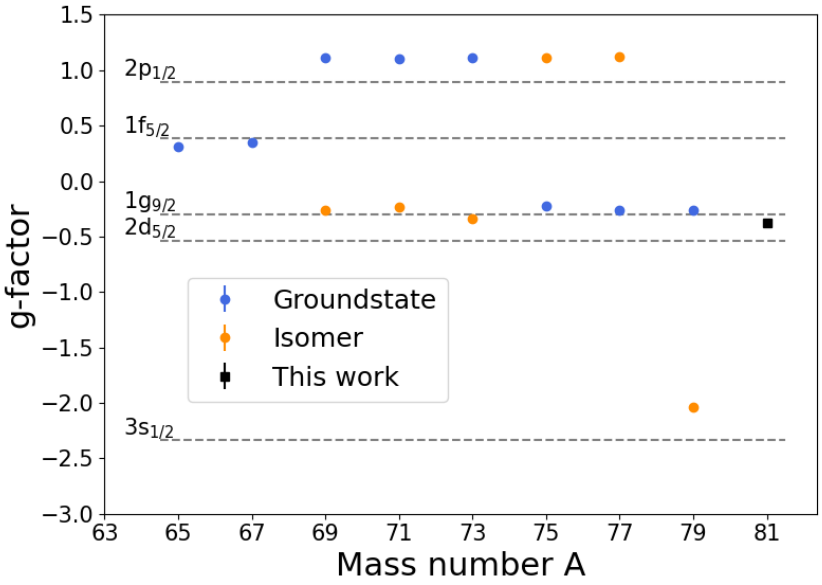

Figure 6.4: *An overview of g-factors of the isotopic chain of Zn from the work of COLLAPS [13] and this work. The dashed lines represent the single particle g-factors of different states.*

These particle-hole excitation configurations result in a more deformed nucleus. Therefore, the quadrupole moment is investigated as well. The calculation of the quadrupole moment of ^{81}Zn is done using equation 3.19. Again, a reference isotope is needed with a well-known quadrupole moment Q_{ref}, and as such ^{67}Zn is chosen to be the reference once more. For the same reason as for the calculation of the magnetic moment, B_{ref} is

taken from COLLAPS [13] and Q_{ref} from [43]. This results in the following quadrupole moment:

$$Q = (-0.29 \pm 0.07)b$$

The negative sign of the quadrupole moment points to an oblate deformation of the nucleus. The error is rather large, and is due to the large error on B_{ref}. A further investigation is also needed for this obtained quadrupole moment along the N=51 isotone chain and should be compared to shell model [33] and ab-initio [44] calculations. In figure 6.5, the experimental quadrupole moments along the N=51 isotone chain are plotted. Due to the substantial uncertainty on the quadrupole moment of ^{81}Zn, it is not possible to draw definitive conclusions.

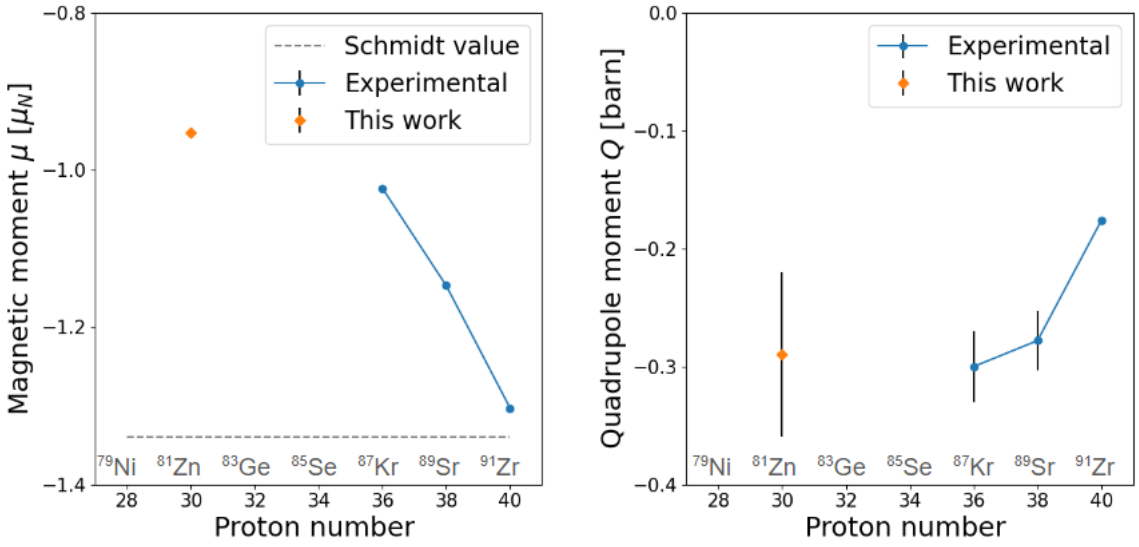

Figure 6.5: *The magnetic moments (left) and quadrupole moments (right) for the N=51 isotone chain. The data points of the experimental values are taken from [17], [26], [8], [25].*

6.2 Nuclear Charge Radii

6.2.1 Isotope Shifts

Isotope shifts in atomic spectra represent subtle variations in the electronic energy levels of different isotopes of the same element. These shifts are critical in both atomic and nuclear physics, prompting extensive theoretical and experimental investigations. When atomic spectra exhibit hyperfine structure, the isotope shift is related to the centroid of the spectral lines. From a nuclear physics standpoint, isotope shifts serve as precise probes for examining nuclear structure. They are particularly valuable for nuclear-model-independent determination of differences in nuclear mean square charge radii, thereby providing significant insights into nuclear properties.

These isotope shifts are calculated by taking the difference between the mean centroid of the scans from isotope with mass number A and the mean centroid of the reference isotope ^{70}Zn, as discussed in previous chapter:

$$\delta\nu^{A,70} = \langle\nu^{A}\rangle - \langle\nu^{70}\rangle \tag{6.1}$$

By using this notation, all isotope shifts of isotopes lower in the isotopic chain than the reference one are negative, and all isotope shifts of isotopes further in the isotopic chain are positive. The error on the isotope shift is a weighted error except for isotopes ^{74}Zn, ^{76}Zn, ^{78}Zn, and ^{82}Zn. For these isotopes, the error on the mean centroid is chosen to be the same as for the reference centroid, namely 2.6 MHz. This error represents the Gaussian distributed standard deviation over the whole experiment and can thus be assigned to these centroids. A weighted mean for isotopes ^{74}Zn, ^{76}Zn, and ^{78}Zn is not appropriate as they only have two scans to calculate the mean centroid and because of a larger reduced chi-square of the fits of the hyperfine spectra. The scans of ^{82}Zn, on the other hand, suffered from a very low count rate. This leads to a smaller reduced chi-square for the fit. To account for this, a larger error is assigned to the mean centroid. In table 6.2, an overview of the calculated isotope shifts can be found with the assigned errors.

6.2.2 King Plot

To calculate the differences in nuclear mean square charge radii, a King plot should be executed. In this way, they can be calculated from the isotope shifts, and the mass and field shift. The isotope shift is related to the differences in nuclear mean square charge radii by the following equation, using ^{70}Zn as the reference isotope:

$$\delta\nu^{A,70} = M \cdot \frac{m_A - m_{70}}{m_A \cdot m_{70}} + F \cdot \delta\langle r^2\rangle^{A,70}$$

with M the mass shift and F the field shift. The King plot method uses stable isotopes from which the differences in nuclear mean square charge radii are well-known, with respect to a reference isotope. In this dissertation, ^{64}Zn, ^{66}Zn, and ^{68}Zn are used to do so, with respect to ^{70}Zn, using muonic data from Fricke [27]. Using this data, represented in table 6.1, a King fit can be executed using the next formula:

$$\frac{\delta\nu^{A,70}}{\mu} = M + F \cdot \frac{\delta\langle r^2\rangle^{A,70}}{\mu}$$

From this linear fit, the mass and field shift are obtained, which then is used to relate the calculated isotope shifts of the other zinc isotopes to the differences in mean square charge radii.

[3]Data for nuclear masses are taken from NUBASE2020.

Table 6.1: *Table with all data needed to perform the King fit.*

$A-70$	$\delta\nu^{A,70}$ [MHz]	$\delta\langle r^2\rangle^{A,70}$ $[fm^2]$	m_A [amu]^3
64-70	-152.54 ± 2.82	-0.4573 ± 0.010	63.9291418
66-70	-96.58 ± 2.84	-0.2947 ± 0.009	65.9260336
68-70	-53.10 ± 2.61	-0.1566 ± 0.008	67.9248442

The field shift is fixed at $F = 324(3)$ MHz$/fm^2$, calculated by Leonid FS-RCCSDT. The mass shift M is set as a free parameter. The result of this fit can be seen in figure 6.6 with:

$$F = 324(3) \text{ MHz}/fm^2$$

$$M = 2873(927) \text{ MHz} \cdot \text{amu} \ = 2.9(9) \text{ GHz} \cdot \text{amu}$$

The reduced chi-square of this fit is rather low, namely $\chi^2_\nu = 0.12$. This is a consequence of the large error bars on the data points combined with the fact that only three data points are used for the fit. However, this fit is considered good as the errors on the fitted parameters are physical and even improved, compared to the results of COLLAPS ($F = 346(35)$ MHz$/fm^2$ and $M = 49(17)$ GHz $\cdot$ amu [16]), where the field shift F was also fixed, taking into account MCDHF calculations.

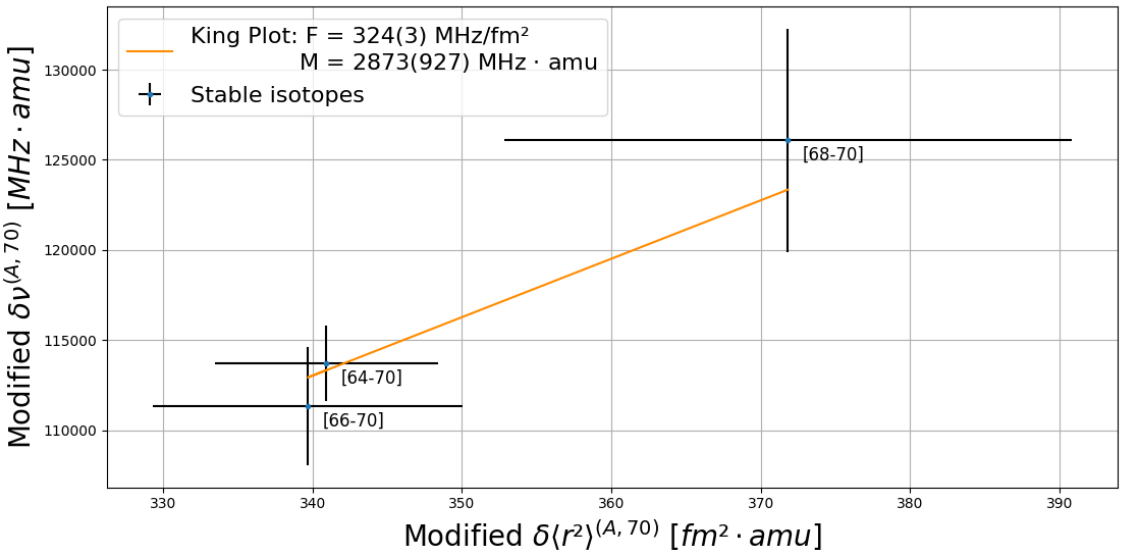

Figure 6.6: *King plot with fixed field shift F and letting the mass shift M free.*

6.2.3 Differences in Mean Square Charge Radii

The zinc isotopes are studied via a $3P_2 \rightarrow 3S_1$ (481.1 nm) transition, and have been investigated already in an earlier study by COLLAPS using the same transition [16]. The results of the differences in mean square charge radii of this project are tabulated in table 6.2. A representation alongside the neutron number is shown in figure 6.7 together with the differences in charge radii of the ground states of Ga and Cu isotopes. Moreover, a comparison of the differences in charge radii is made with the ones obtained from COLLAPS [16]. A good agreement between the differences in charge radii from this work and from COLLAPS is observed with the addition of two extra data points crossing N=50.

From the trend of $\delta\langle r^2\rangle$ for the zinc isotopic chain, two main observations can be made. The first one is an increase in charge radii with the neutron number. This phenomenon is accounted for by the liquid drop model for almost all elements with atom number higher than iron which can be seen in the table of experimental nuclear ground state charge radii by I. Angeli and K.P. Marinova [30]. The second observation is the clear kink at $N = 50$, a variation in the slope of $\delta\langle r^2\rangle$ which is associated with the presence of magic numbers. In isotopic chains, the slope of $\delta\langle r^2\rangle$ becomes steeper immediately after a magic number, while it stagnates just before a magic number. In this case, the magic number is $N = 50$, which is in line with the magic numbers predicted by the shell model.

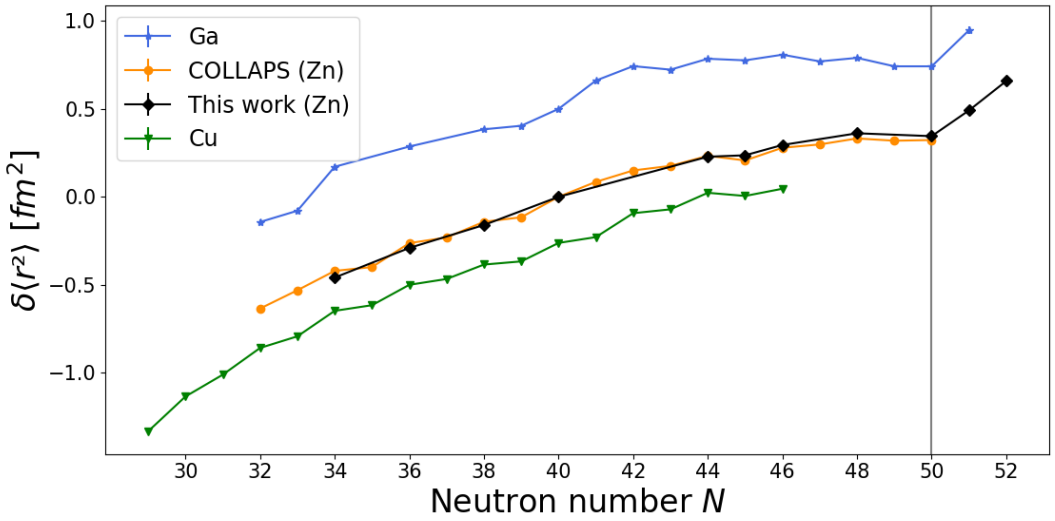

Figure 6.7: *Plot of differences in nuclear mean square charge radii from this work next to those of different isotopic chains, data taken from [24], [19], and [16]. The isotope chains have a relative offset of 0.5 fm^2 for clarity, except for the Zn chain for comparison between this work and the results from COLLAPS (only ground states).*

Table 6.2: *Overview of all obtained results for the isotope shifts $\delta\nu_{exp}^{A,70}$ and the differences in the mean square charge radii $\delta\langle r^2\rangle_{exp}^{A,70}$. The latter result from the King Plot method, and are compared next to the results of COLLAPS $\delta\langle r^2\rangle_{COLLAPS}^{A,70}$.*

A	I	$\delta\nu_{exp}^{A,70}$ [MHz]	$\delta\langle r^2\rangle_{exp}^{A,70}$ $[fm^2]$	$\delta\langle r^2\rangle_{COLLAPS}^{A,70}$ $[fm^2]$
64	0	-152.54 ± 2.82	-0.459 ± 0.010	-0.421 ± 0.005
66	0	-96.58 ± 2.84	-0.290 ± 0.009	-0.263 ± 0.005
68	0	-53.10 ± 2.61	-0.160 ± 0.008	-0.142 ± 0.003
74	0	76.12 ± 3.68	0.228 ± 0.012	0.233 ± 0.005
75	7/2	79.31 ± 3.68	0.236 ± 0.012	0.207 ± 0.004
75^m	1/2	83.96 ± 3.68	0.251 ± 0.012	0.231 ± 0.007
76	0	98.27 ± 3.68	0.293 ± 0.012	0.279 ± 0.005
78	0	120.35 ± 3.68	0.358 ± 0.012	0.332 ± 0.004
80	0	116.01 ± 2.68	0.342 ± 0.010	0.323 ± 0.005
81	5/2	164.35 ± 3.68	0.450 ± 0.013	/
82	0	218.99 ± 3.68	0.657 ± 0.013	/

The kink can further be investigated by calculating its kink parameter. This is a parameter quantifying the steepness of the kink by the following equation obtained from [14]:

$$\Delta^3(\delta\langle r^2\rangle, N) = -\delta\langle r^2\rangle^N + \frac{1}{2}(\delta\langle r^2\rangle^{N-2} + \delta\langle r^2\rangle^{N+2}) \tag{6.2}$$

Using the differences in charge radii from this work, found in table 6.2, this kink parameter equals $\Delta^3(\delta\langle r^2\rangle, 50) = 0.166 \pm 0.013\ fm^2$. At each magic neutron number, a same strength of this kink parameter is expected along different isotopic chains. Looking at krypton (Z=36) [17], rubidium (Z=37) [12], and strontium (Z=38) [26], their kink parameters are nearly equal within the range of their uncertainties (values are reported in table 6.3). This leads to the conclusion that there is a very stable kink parameter in the N=50 region. These elements, however, have proton numbers that are slightly higher than zinc. Ideally, the kink of isotopic chains around Z=30 can be investigated as well. At this moment, no such study can be performed since experiments of gallium or copper chains do not reach as far in neutron number. Moreover, experiments with arsenic (Z=33), selenium (Z=34), and bromine (Z=35) are very difficult to conduct as these elements are very chemically reactive.

The kink parameter at N=50 can be compared to kinks at different magic neutron numbers. F. Sommer et al. [14] investigated this kink parameter at the N=28 shell closure for isotonic chains for all elements for which the charge radii have been measured for

N=26, 28, 30. Their finding was that the experimental kink parameters $\Delta^3(\delta\langle r^2\rangle, 28)$ are almost identical for K, Ca, and Ni and slightly larger for Mn and Fe. These larger values are explained by the contributions of ground state quadrupole correlations in these open-proton-shell nuclei. This study also analyzed the kink parameter at N=28 for the doubly magic ^{48}Ca and ^{56}Ni. The result is an almost equal size of $\Delta^3(\delta\langle r^2\rangle, 28)$ for Z=20 and Z=28, despite the differences in size of the neutron shell gap, different charges, and different types of shell closures. To follow up on the work of F. Sommer et al., an additional study is performed, investigating the kink parameter in all shell closure regions.

Firstly, the kink parameter is recalculated for the N=28 shell closure region. F. Sommer et al. investigated the kink of the charge radii, this study however focuses on the kink of the differences in mean square charge radii. The values of the kink parameter are thus not the same, but the relative proportions should remain unchanged. In table 6.3, the kink parameters for potassium, calcium, iron, and nickel are reported, using data from [9], [21], [32], and [14] respectively. The same findings as in the study of F. Sommers et al. are observed. The values of the kink parameters of these four isotopes are almost equal in size, with a higher value for iron.

Moreover, the kink parameter for isotopic chains crossing N=82 are obtained for tin, cesium, barium and cerium, again reported in table 6.3, using data from [4], [5], [37], and [11] respectively. In this region, the kink parameter is also not completely stable anymore. Larger deviations are observed, and in particular tin and barium can be seen as the lower and upper outliers respectively. The small size of the kink parameter for tin can be explained by its doubly-magic character, resulting in a more spherical nucleus with a smaller kink parameter. However, similar to the N=28 region, the value of the kink parameter is rather constant within error bars.

Table 6.3: *Overview of all calculated kink parameters of different isotopic chains in the different shell closure regions.*

Kink parameter $\Delta^3(\delta\langle r^2\rangle, N)$ $[fm^2]$					
N=28		N=50		N=82	
K_{19}	0.209(12)	Zn_{30}	0.166(13)	Sn_{50}	0.080(23)
Ca_{20}	0.209(4)	Kr_{36}	0.162(2)	Cs_{55}	0.111(1)
Fe_{26}	0.299(7)	Rb_{37}	0.170(2)	Ba_{56}	0.139(1)
Ni_{28}	0.227(5)	Sr_{38}	0.164(2)	Ce_{58}	0.124(1)

Ideally, the region of N=126 shell closure is also explored since a kink is observed there as well. At present, this is not possible as only one isotopic chain, namely lead, contains enough data to calculate the kink parameter. Others, like francium and radon, do cross the N=126 shell gap, but the differences in charge radii are not determined around the shell closure.

Furthermore, these different regions are compared to each other in figure 6.8. Firstly, a very stable kink parameter is noted in the N=50 region. Secondly, a global trend in the size of the kink parameter between the different regions is observed. Moving from N=28 to N=82, the size of the kink parameter decreases. Including the kink parameter for lead at the N=126 shell closure[4], $\Delta^3(\delta\langle r^2\rangle, 126) = 0.046 \pm 0.001\ fm^2$, this trend is further confirmed. However, it is important to note that this value may be an outlier in the N=126 region and should be interpreted with caution. Nevertheless, the kink parameter $\Delta^3(\delta\langle r^2\rangle, 126)$ for lead is half in size compared to the tin outlier in the N=82 region. Although more data is needed to make a definitive conclusion and to fully include the N=126 region, a decreasing trend in the size of the kink parameter is observed when going to higher shell closures. Further investigation of the deformation in the different regions can shed more light on this decreasing behavior.

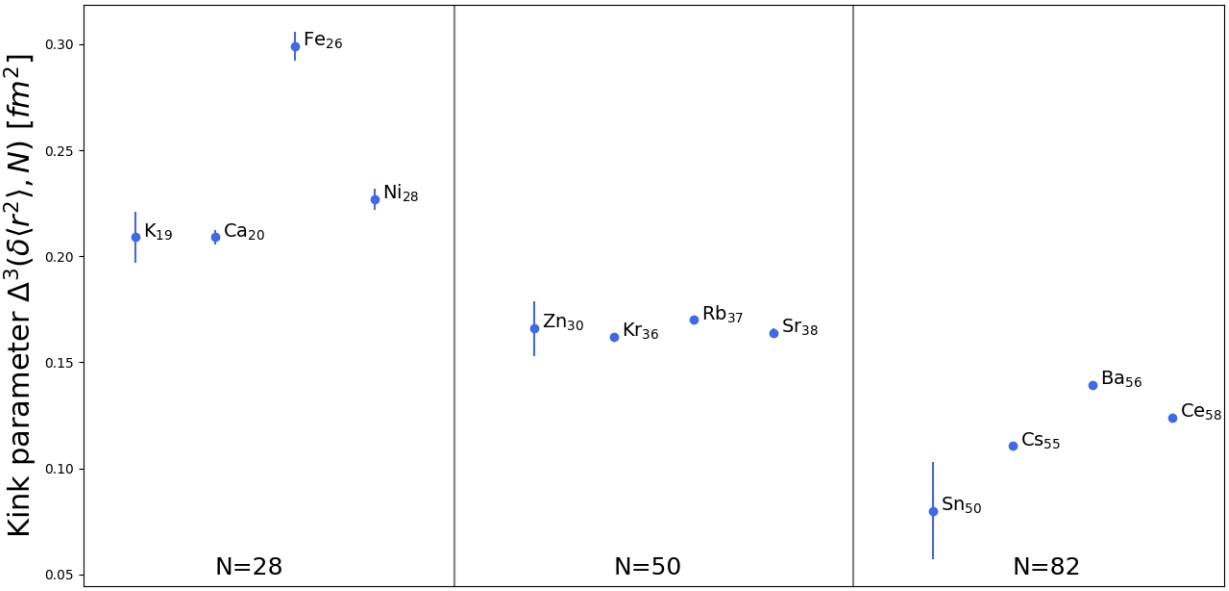

Figure 6.8: *The size of the kink parameter in different shell closure regions. The region of N=126 is not included as currently, not enough data is available.*

[4]Data obtained from [34].

Chapter 7

Conclusion and Future Perspectives

The collinear resonance ionization spectroscopy method at ISOLDE has proven to be a successful technique to probe the hyperfine structure of neutron-rich zinc isotopes with a high resolution. Studying these exotic nuclei can be seen as a benchmark for testing the rigidity of magic numbers.

The hyperfine spectra of zinc isotopes from ^{64}Zn to ^{80}Zn have been studied before by COLLAPS [16], [13]. In this work, ^{81}Zn and ^{82}Zn are investigated in addition, making it possible to investigate the nuclear charge radii crossing N=50. Furthermore, the spin and nuclear moments of ^{81}Zn are obtained.

The spin of ^{81}Zn was still in debate as shell model calculations expected a degeneracy for the ground state of the $1/2^+$ and $5/2^+$ state, and from experiments, a lowering of the excited $1/2^+$ state was observed. In this work, the spin is assigned to be $5/2^+$, resulting in no flipping of states. This is the first time that the spin is determined this close to ^{79}Ni. Furthermore, the magnetic moment and the g-factor of ^{81}Zn are calculated: $\mu = (-0.9522 \pm 0.0028)\mu_N$, and $g = -0.3809 \pm 0.0011$. The study of the g-factor and the magnetic moment leads to a possibility of configuration mixing. More investigation is necessary to compare the magnetic moment of the possible configurations with the one obtained from this experiment and with theoretical calculations. Moreover, these configurations require a more deformed nucleus. Therefore, the quadrupole moment of ^{81}Zn is extracted as well: $Q = (-0.29 \pm 0.07)$b. Because the uncertainty on this value is quite big, no real conclusion can be made. More investigation is needed here as well, by comparing the experimental value with the one obtained from theoretical calculations.

Lastly, the isotope shifts were obtained. Using the King plot method, the differences in nuclear mean square charge radii could be derived from these isotope shifts. The charge radii are compared to the ones obtained by COLLAPS [16] and a good agreement in the trend is remarked. Furthermore, a strong kink is observed, proving a strong shell closure at N=50. In addition, the kink parameter is investigated in different regions of shell closure. The size of this kink parameter is rather constant in each region, however, a decreasing trend in size is observed when going to higher shell closures. Further investigation on the deformation around the shell closure can shed light on the reason for this trend.

From the results of this dissertation, further investigation into the nuclear moments can be performed. This could lead to a more precise determination of the quadrupole moment, enhancing our understanding of the deformation of ^{81}Zn crossing the N=50 shell closure. Moreover, deriving the magnetic moments for the possible configurations and comparing them to the experimentally obtained magnetic moment will provide deeper insights into the configuration of ^{81}Zn.

Appendix A

Observed Fluctuations

A.1 ISCOOL Voltage Fluctuations

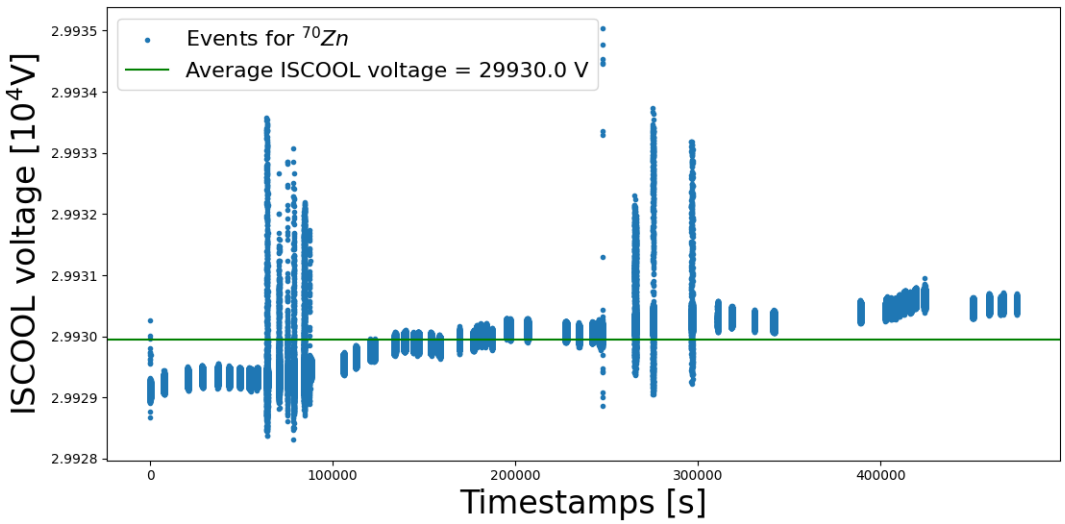

Figure A.1: *Fluctuations in voltage of ISCOOL during all reference scans over time. Each vertical 'line' represents a scan, which is a bundle of events that experiences fluctuations in voltage.*

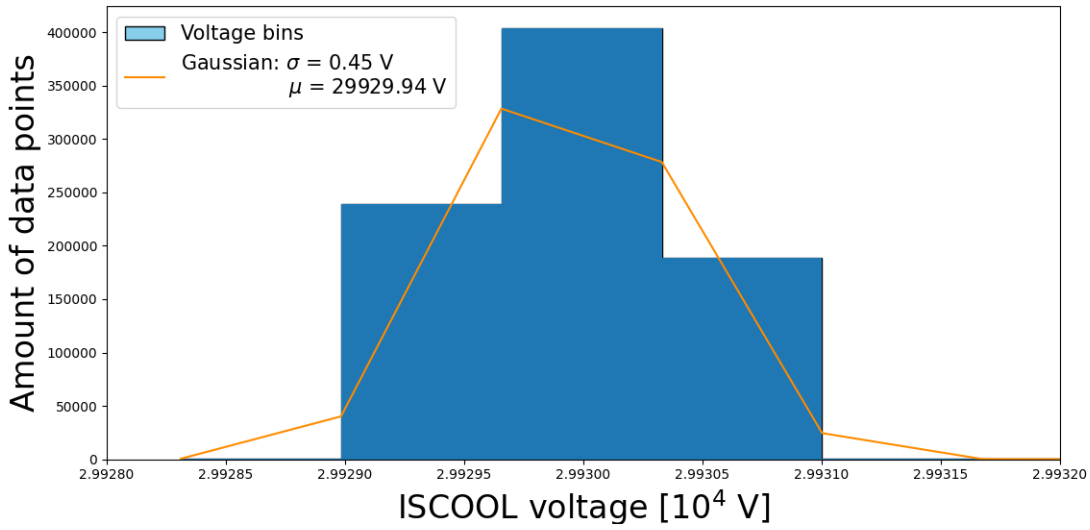

Figure A.2: *Gaussian fit of the ISCOOL voltage histogram.*

A.2 Diode Wavenumber Fluctuations

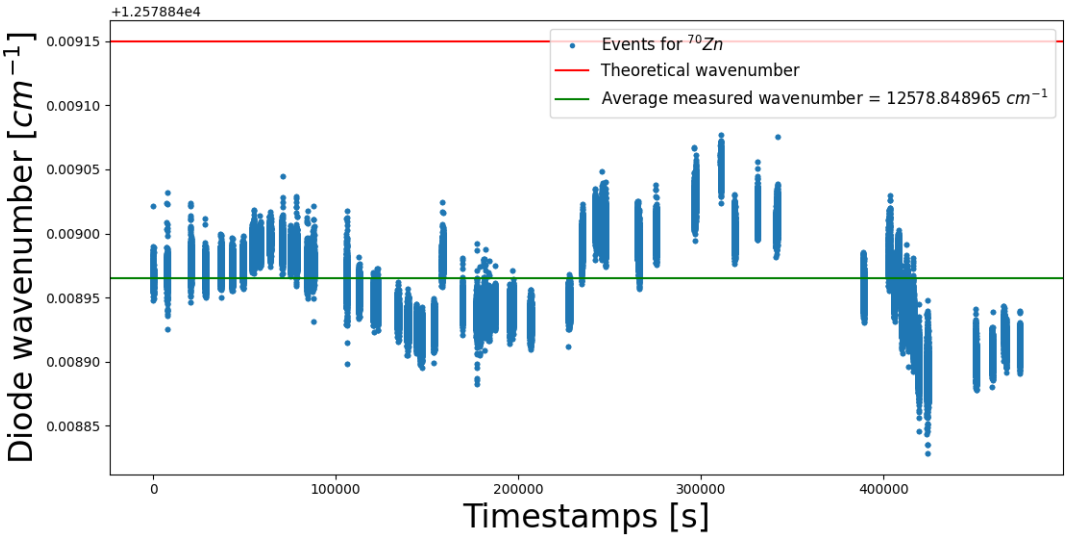

Figure A.3: *Diode wavenumbers of all events during all reference scans over time. Each vertical 'line' represents a scan, which is a bundle of events that shift in wavenumber.*

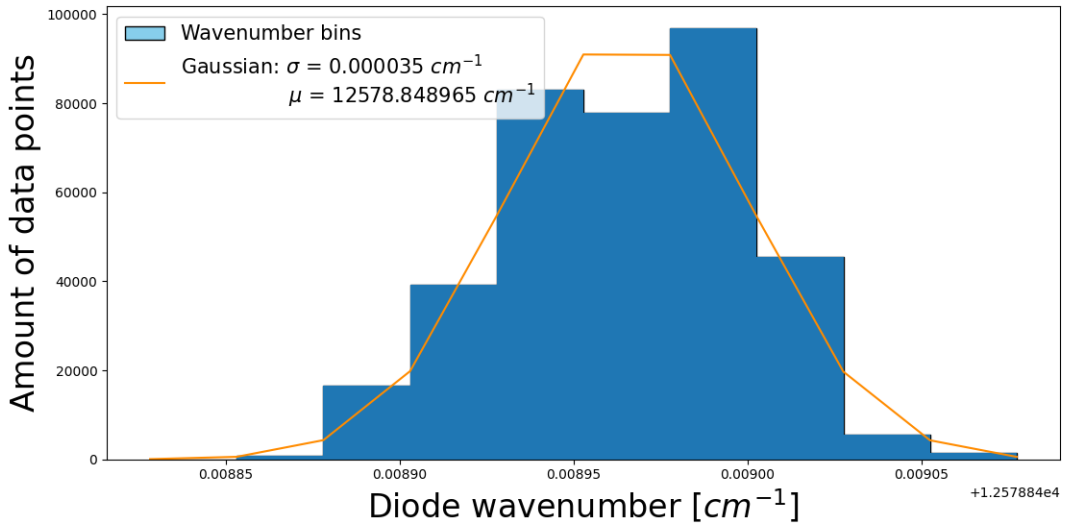

Figure A.4: *Gaussian fit of the diode wavenumber histogram.*

Bibliography

[1] ISOLDE logos, layouts and templates. `https://isolde.web.cern.ch/isolde-logos-layouts-and-templates`. Accessed at 5/06/2024.

[2] I.P. Aliseda. *ISCOOL project: cooling and bunching RIBs for ISOLDE*. PhD thesis, ISOLDE, CERN, 2006.

[3] T.E. Cocolios B. Cheal and S. Fritzsche. Laser spectroscopy of radioactive isotopes: Role and limitations of accurate isotope-shift calculations. *Physical Review A*, 86(4), 2012.

[4] L.V. Rodríguez C. Gorges et al. Laser spectroscopy of neutron-rich tin isotopes: A discontinuity in charge radii across the N=82 shell closure. *Physical Review Letters*, 122, 2019.

[5] F. Touchard C. Thibault et al. Hyperfine structure and isotope shift of the d2 line of 118-145Cs and some of their isomers. *Nuclear Physics*, A367, 1981.

[6] R. Casten. Nuclear structure from a simple perspective. *Oxford University Press on Demand*, 23, 2000.

[7] R.P. de Groote. *High resolution collinear resonance ionization spectroscopy of neutron-rich 76,77,78Cu isotopes*. PhD thesis, PhD thesis at IKS KULeuven, 2017.

[8] J. Oeser E. Brun and H.H. Staub. Magnetic moment and spin of 91Zr. *Physical Review*, 105, 1957.

[9] A. Koszorús et al. Charge radii of exotic potassium isotopes challenge nuclear theory and the magic character of N=32. *Nature Physics*, 17:439–443, 2021.

[10] Alok K. Singh et al. Observation of the nuclear magnetic octupole moment of 173 Yb from precise measurements of the hyperfine structure in the 3P2 state. *Physical Review A*, 87, 2013.

[11] B. Cheal et al. Collinear laser spectroscopy of neutron-rich cerium isotopes near the N=88 shape transition. *Journal of Physics G: Nuclear and Particle Physics*, 29, 2003.

[12] C. Thibault et al. Hyperfiae structure and isotope shift of the D2 line of 76-98Rb and some of their isomers. *Physical Review C*, 23, 1981.

[13] C. Wraith et al. Evolution of nuclear structure in neutron-rich odd-Zn isotopes and isomers. *Physics Letters B*, 771:385–391, 2017.

[14] F. Sommer et al. Charge radii of 55,56Ni reveal a surprisingly similar behavior at N=28 in Ca and Ni isotopes. *Physical Review Letters*, 129, 2022.

[15] K. Sieja et al. Shell model description of zirconium isotopes. *Physical Review C*, 79, 2009.

[16] L. Xie et al. Nuclear charge radii of 62-80Zn and their dependence on cross-shell proton excitations. *Physics Letters B*, 797, 2019.

[17] M. Keim et al. Laser-spectroscopy measurements of 72–96Kr spins, moments and charge radii. *Nuclear Physics A*, 586, 1995.

[18] M. Stanoiu et al. N=14 and 16 shell gaps in neutron-rich oxygen isotopes. *Physical Review C*, 69, 2004.

[19] M.L. Bissell et al. Cu charge radii reveal a weak sub-shell effect at N=40. *Physical Review C*, 2016.

[20] R. Taniuchi et al. 78Ni revealed as a doubly magic stronghold against nuclear deformation. *Nature*, 569:53–58, 2019.

[21] R.F. Garcia Ruiz et al. Unexpectedly large charge radii of neutron-rich calcium isotopes. *Nature Physics*, 12, 2016.

[22] T.E. Cocolios et al. High-resolution laser spectroscopy with the collinear resonance ionisation spectroscopy (CRIS) experiment at CERN-ISOLDE. *Nuclear Instruments and Methods in Physics Research Section B: Beam Interactions with Materials and Atoms*, 376:284–287, 2016.

[23] T.J. Procter et al. Development of the CRIS (collinear resonant ionisation spectroscopy) beam line. *Journal of Physics: Conference Series*, 381, 2012.

[24] T.J. Procter et al. Nuclear mean-square charge radii of 63,64,66,68-82Ga nuclei: No anomalous behavior at N=32. *Physical Review C*, 86, 2012.

[25] Vladimir Kellö et al. The nuclear quadrupole moment of 91Zr from molecular data for ZrO and ZrS. *Chemical Physics Letters*, 318, 2000.

[26] E.B. Ramsay F. Buchinger. Systematics of nuclear ground state properties in 78–100Sr by laser spectroscopy. *Physical Review C*, 41, 1990.

[27] G. Fricke and Landolt-Börnstein Group I Elementary Particles K. Heilig. Nuclei and atoms 20 (nuclear charge radii). *SpringerMaterials*, 2024.

[28] K. Heilig G. Fricke. Nuclear charge radii. *Springer Berlin*, 2004.

[29] G. R. Jansen G. Hagen and T. Papenbrock. Structure of 78Ni from first-principles computations. *Physical Review Letters*, 117, 2016.

[30] K.P. Marinova I. Angeli. Table of experimental nuclear ground state charge radii: An update. *Atomic Data and Nuclear Data Tables*, 99:69–95, 2013.

[31] P.C. Srivastava K. Maurya and I. Mehrotra. Shell model description of N=51 isotones. *IOSR Journal of Applied Physics*, 3, 2013.

[32] D.M. Rossi K. Minamisono et al. Charge radii of neutron deficient 52,53Fe produced by projectile fragmentation. *Physical Review Letters*, 117, 2016.

[33] J.G. Li. Merging of the island of inversion at N=40 and N=50. *Physics Letters B*, 840, 2023.

[34] W. Faubel M. Anselment et al. The odd-even staggering of the nuclear charge radii of Pb isotopes. *Nuclear Physics*, 1451, 1986.

[35] S.W. Bai M. Athanasakis et al. Probing the magicity and shell evolution in the vicinity of N=50 with high-resolution laser spectroscopy of 81,82Zn isotopes. *CERN-INTC-2020-064 / INTC-P-579*, 2020.

[36] J.R. Reilly M. Athanasakis-Kaklamanakis et al. Voltage scanning and technical upgrades at the collinear resonance ionization spectroscopy experiment. *Nuclear Instruments and Methods in Physics Research Section B*, 541:86–89, 2023.

[37] A.M. Martensson-Pendrill and A. Ynnerman. Isotope shift and nuclear charge radii of barium isotopes. *Journal of Physics B: Atomic, Molecular and Optical Physics*, 25, 1992.

[38] M.G. Mayer. On closed shells in nuclei. *Physical Review*, 75, 1949.

[39] H. Miyazawa. Deviations of nuclear magnetic moments from the Schmidt lines. *Progress of Theoretical Physics*, IV, 1951.

[40] R. Neugart and G. Neyens. Nuclear moments. *Springer, Berlin Heidelberg*, page 135–189, 2006.

[41] J.H.D. Jensen O. Haxel and H.E. Suess. On the "magic numbers" in nuclear structure. *Physical Review*, 75, 1949.

[42] T. Otsuka. Shell structure of exotic nuclei. *Lecture Notes in Physics 764*, page 1–25, 2009.

[43] N. Stone. *International Nuclear Data Committee*, 0658:1–171, 2014.

[44] S.R. Stroberg. Nucleus-dependent valence-space approach to nuclear structure. *Physical Review Letters*, 118, 2017.

[45] B. van den Borne W. Gins et al. SATLAS2: An update to the package for analysis of counting data. *Computer Physics Communications*, 297, 2024.

Department of Physics and Astronomy
Celestijnenlaan 200d bus 2412
3001 LEUVEN, BELGIË
tel. + 32 16 32 71 24
www.kuleuven.be